The Astrophysical Journal, 763:59 (19pp), 2013 January 20 doi:10.1088/0004-637X/763/1/59

X-RAY SELECTED AGN HOST GALAXIES ARE SIMILAR TO INACTIVE GALAXIES OUT TO $z = 3$: RESULTS FROM CANDELS/CDF-S

D. J. Rosario[1], M. Mozena[2], S. Wuyts[1], K. Nandra[1], A. Koekemoer[3], E. McGrath[4], N. P. Hathi[5], A. Dekel[6], J. Donley[7], J. S. Dunlop[8], S. M. Faber[2], H. Ferguson[3], M. Giavalisco[9], N. Grogin[3], Y. Guo[9], D. D. Kocevski[10], D. C. Koo[2], E. Laird[11], J. Newman[12], C. Rangel[11], and R. Somerville[13]
[1] Max-Planck-Institute for Extraterrestrial Physics, Garching, D-85748, Germany
[2] Astronomy Department and UCO-Lick Observatory, University of California, Santa Cruz, CA 95064, USA
[3] Space Telescope Science Institute, Baltimore, MD 21218, USA
[4] Department of Physics, Colby College, Waterville, ME 04901, USA
[5] Observatories of the Carnegie Institution of Washington, Pasadena, CA 91101, USA
[6] Racah Institute of Physics, The Hebrew University, Jerusalem 91904, Israel
[7] Los Alamos National Laboratory, Los Alamos, NM 87545, USA
[8] Institute for Astronomy, Royal Observatory, Edinburgh EH9 3HJ, UK
[9] Department of Astronomy, University of Massachusetts, Amherst, MA 01003-9305, USA
[10] Department of Physics and Astronomy, University of Kentucky, Lexington KY 40506-0055, USA
[11] Department of Physics, Imperial College, London SW7 2AZ, UK
[12] Department of Physics and Astronomy, University of Pittsburgh, Pittsburgh, PA 15260, USA
[13] Department of Physics & Astronomy, Rutgers University, Piscataway, NJ 08854, USA
Received 2011 December 16; accepted 2012 November 23; published 2013 January 8

ABSTRACT

We use multi-band spatially resolved photometry from the Cosmic Assembly Near-IR Deep Legacy Survey in the 4 Ms Chandra Deep Field-South to explore the nuclear and extended colors, color gradients, and stellar populations of the host galaxies of X-ray selected active galactic nuclei (AGNs) out to $z = 3$. Based on a study of their central light, we develop X-ray based criteria to exclude objects with strong AGN contamination. We use stellar masses from the FIREWORKS database to understand and account for stellar mass selection effects and carefully study, for the first time, the resolved host galaxy properties of AGNs at $z \sim 2$ in their rest-frame optical light without substantial nuclear contamination. AGN hosts span a sizable range of stellar masses, colors, and color gradients at these redshifts. Their colors, color gradients, and stellar population properties are very similar to inactive galaxies of the same stellar mass. At $z \sim 1$, we find a slightly narrower range in host colors compared to inactive galaxies, as well as hints of more recent star formation. These differences are weaker or non-existent among AGN hosts at $z \sim 2$. We discuss the importance of AGN-driven feedback in the quenching of galaxies at $z \gtrsim 1$ and speculate on possible evolution in the relationship between black hole accretion and the host galaxy toward high redshifts.

Key words: galaxies: active – galaxies: photometry – infrared: galaxies – surveys – X-rays: galaxies

Online-only material: color figures

1. INTRODUCTION

Active galactic nuclei (AGNs) are the result of accretion onto supermassive black holes (SMBHs), which are generally found in the centers of massive galaxies. Till quite recently, activity in galactic nuclei was studied as a topic of special interest, usually unrelated to the evolution of galaxies. This has changed in the last decade as tight scaling relationships were uncovered between the masses of SMBHs and the masses of their host spheroids (e.g., Magorrian et al. 1998; Ferrarese & Merritt 2000; Gebhardt et al. 2000). These relationships seem to imply a close connection between the evolution of nuclear black holes and the evolution of galaxies as a whole (but see Jahnke & Macciò 2011). Such a connection is, at first glance, quite remarkable, since the typical sphere of influence of even the largest black holes is less than a few tens of parsecs in size, more than three orders of magnitude smaller than the typical sizes of galaxies. However, since the inflow of gas to the black hole is the key driver of SMBH growth and this depends on the circumnuclear environment and the large-scale properties of the host galaxy (e.g., its gas content), an essential connection between black hole growth and host galaxy properties may arise through the fueling of SMBHs.

Another avenue through which nuclear activity can influence the host galaxy, despite the large difference in spatial scales, is through a set of physical processes collectively called "feedback." Examples include energy- and momentum-driven outflows in QSOs (Pounds et al. 2003), outflows accelerated by relativistic jets (Morganti et al. 2005; Rosario et al. 2010), and the suppression of cluster cooling flows by radio lobes (McNamara & Nulsen 2007).

AGN feedback can play an important role in galaxy evolution by driving and regulating the transformations of star-forming galaxies into quiescent galaxies. Strong feedback from powerful AGNs can eject gas from their host galaxies, effectively shutting down star formation and moving them onto the Red Sequence (Schawinski et al. 2007; Hopkins et al. 2008a; Kaviraj et al. 2011). In addition, feedback can prevent star formation by keeping enough gas from cooling and accreting onto these galaxies, thereby keeping them on the Red Sequence. AGN feedback has become an essential element of several modern semianalytic models of galaxy formation (Bower et al. 2006; Croton et al. 2006; Somerville et al. 2008; Cattaneo et al. 2009), since it curtails the formation of very high mass blue galaxies, as required by observations (Benson et al. 2003). The similarity between the timescale estimates of AGN activity and

the quenching of star formation also lends some credence to the relevance of AGN feedback (Bundy et al. 2008).

Several studies have searched for an empirical signature of AGN feedback; however, there is a lack of sufficient evidence for wide-spread AGN-driven outflows at the level needed to satisfy the requirements of most semianalytic models (Tadhunter 2008), except in perhaps the most powerful AGNs and in ultra-luminous infrared galaxies (Rupke & Veilleux 2011; Sturm et al. 2011). This may be because evolutionary models invoke a feedback prescription that is too strong, or it may be because outflows are rather transient events and difficult to characterize. An alternate approach has been to search for a direct link between the strength of nuclear activity and the transformation of the galaxy on larger scales by the examination of the structure and star formation histories (SFHs) of AGN host galaxies. While indirect, these methods are more general and can be applied to large galaxy samples across a range of redshifts.

In the local universe, AGNs tend to be preferentially in galaxies that lie between the two peaks of the bi-modal galaxy color distribution, i.e., they tend to be hosted by so-called Green Valley galaxies (Kauffmann et al. 2003; Schawinski et al. 2009). This trend is found among X-ray selected AGNs even out to $z \sim 2$ (Silverman et al. 2008; Nandra et al. 2007; Brusa et al. 2009). Galaxies in the Green Valley are generally believed to be transitioning from a state of ongoing star formation toward quiescence (but see Silverman et al. 2008). Therefore, the overrepresentation of AGNs in the Green Valley is taken as evidence of the influence of the AGN in the suppression of star formation, though some doubts remain about the generality of this interpretation (Xue et al. 2010; Cardamone et al. 2010).

Morphologically, local low-luminosity AGNs are found in disk galaxies with substantial bulge components, i.e., early-type disks (Whittle 1992; Hunt & Malkan 1999; Schawinski et al. 2010). There is, however, considerable scatter in the distribution of AGN host morphologies: a large proportion, as much as 30%, have late-type spiral morphologies. Such trends are found among AGN hosts even out to $z \sim 2$ (Pierce et al. 2007; Georgakakis et al. 2009; Gabor et al. 2009; Schawinski et al. 2011; Kocevski et al. 2012) and suggest that low- and intermediate-luminosity AGNs are not intimately associated with major galaxy mergers, and that secular processes may play an important role in their fueling. The case is not as clear for luminous AGNs, which are rare, typically at higher redshifts and in which contamination from a nuclear point source can complicate the measurement of host galaxy structure. A few careful studies of the hosts of such AGNs suggest a similar distribution of morphological types (Dunlop et al. 2003; Guyon et al. 2006), though with more pronounced signatures of recent galaxy mergers or interactions (Bennert et al. 2008).

Evolutionary studies show that the space density of luminous AGNs peaks at $z \sim 1.5$–2.5 (e.g., Boyle & Terlevich 1998; Hopkins et al. 2007). It is at these redshifts that the most pronounced and widespread signatures of AGN feedback on galaxy populations may be expected. Till recently, detailed studies of AGN host galaxies at these epochs have been hampered by their faintness and the paucity of adequate samples with good redshifts. In addition, at $z > 1.5$, the 4000 Å break, a principal spectral diagnostic feature in the stellar continuum of galaxies, is redward of 1 μm. Imaging of these distant galaxies with high-resolution instruments, such as those on the *Hubble Space Telescope* (*HST*), was generally restricted to the optical bands, which traced the rest-frame near-UV and were most sensitive to the emission from massive stars and recent star formation. Our understanding of the extended stellar populations of AGN hosts at $z \sim 2$ was restricted to that of a handful of objects imaged with the second-generation *HST*/NICMOS camera or through Adaptive Optics instruments on large ground-based facilities.

The near-IR (NIR) channel of the recently commissioned Wide-Field Camera 3 (WFC3) on the refurbished *HST* is greatly enhancing our view of the distant universe by providing unprecedented sensitivity and resolution out to 1.7 μm. In this study, we combine the Chandra Deep Field South (CDF-S) 4 Ms X-ray catalog with multi-band optical and NIR imaging from *HST* Advanced Camera for Surveys (ACS) and WFC3, as well as existing multiwavelength ground-based data sets in the GOODS-S fields. We explore resolved photometry of AGN hosts in the redshift range of $0.5 < z < 3$ and study the properties of their galaxy light without substantial contamination from nuclear AGN emission. We derive rest-frame UV-optical colors and extinctions for these galaxies, constrain their SFHs, and compare these properties to a well-defined comparison sample of inactive galaxies to place the AGN hosts in the context of field galaxy samples over the range of epochs in which most of the growth of SMBHs and stellar mass occurs.

The paper is organized as follows: in Section 2, we introduce the various data sets that we bring to bear in this study; in Section 3, we discuss the selection of an AGN sample and its X-ray properties, as well as the process of defining a control sample of inactive galaxies; in Sections 4 and 5, we introduce the technique of aperture photometry applied to the resolved images of galaxies and the method used to derive various properties such as colors and SFHs. In Section 6, we introduce nuclear colors and define a method to remove objects where AGN light strongly contaminates the extended photometry. Finally, in Sections 7, 8, and 9, we analyze the outer colors, extinctions, color gradients, and SFHs of AGN hosts. We discuss our results in Section 10.

Throughout this work, we adopt a ΛCDM concordance cosmology with $H_0 = 70$ km s^{-1} Mpc^{-1}.

2. DATA SETS

2.1. HST Imaging

The Wide-Field Camera 3 Infrared Channel (WFC3-IR) is a fourth-generation instrument on the *HST*, designed to provide low thermal background diffraction-limited imaging over a relatively wide area ($136'' \times 123''$) in the NIR from 0.8 to 1.7 μm. Details of the instrument and its capabilities can be found in Baggett et al. (2008) and the WFC3 Instrument Handbook.

As part of the CANDELS Multi-Cycle Treasury Survey (Grogin et al. 2011; Koekemoer et al. 2011), the GOODS-S field was imaged with two NIR filters: F125W (approx. *J* band) and F160W (approx. *H* band). The imaging data set consists of a core set of deep exposures (part of CANDELS-Deep) and a shallower extension (CANDELS-Wide). Combined with the archival WFC3 Early Release Science (ERS2) data set (Windhorst et al. 2011), the *J*- and *H*-band imaging covers, in total, 176 arcmin^2. The CANDELS-Deep and ERS2 imaging has an average *H*-band integration of 5 ks, while the CANDELS-Wide extension has a depth of 1.4 ks. The *J*-band images have a similar depth. The individual WFC3-IR exposures were registered, cleaned, and combined with a custom-built MULTIDRIZZLE-based pipeline into a single large mosaic of the GOODS-S field. Details of the survey design, depths, dither patterns, reduction, astrometric and photometric calibration,

and mosaic creation can be found in the principal CANDELS reference publications (Grogin et al. 2011; Koekemoer et al. 2011). For this work, we employed the combined multi-depth mosaic and its associated weight map. In addition to CANDELS WFC3 data, we also use imaging in the short *Y*-band filter (F098M) from the archival ERS2 program.

We also made use of the GOODS ACS v2.0 imaging data set, publicly available from the online GOODS database. Images in four optical filters (F435W, F606W, F775W, and F850LP) were used, with average integrated exposures of 7.2, 5.4, 7.0, and 18.2 ks, respectively. Descriptions of the data set, including reductions and calibrations, can be found on the public GOODS archive and in Giavalisco et al. (2004).

The multi-epoch nature of the CANDELS data set also produces a non-uniform point-spread function (PSF) across the CANDELS mosaic, as subexposures of different depth and orientation are combined at any given pixel location. Detailed modeling of stars indicates that the WFC3 PSF is quite stable across each of the subfields. This is because the WFC3 images for each epoch were generated from tiling patterns with little overlap, ensuring that submosaics from each epoch have uniform depths and most differences between the PSFs in each epoch were a consequence of the changing orientations (Grogin et al. 2011). On the other hand, the PSFs in each of the three subfields differ greatly between themselves. Therefore, we relied on a set of WFC3 PSFs derived for each of the three subfields, one for each band. These representative PSFs were constructed from model PSFs for the center of the WFC3-IR camera, generated by the TinyTim software (Hook et al. 2008), which were then drizzled together using the appropriate dither pattern for the CANDELS submosaics (Koekemoer et al. 2011). Appropriate PSFs for the GOODS ACS mosaics were created in the same way as the WFC3 mosaics. In Section 4, we describe how the PSFs were used to generate kernels to match the resolutions of the *HST* images in the different bands.

2.2. FIREWORKS Photometric Database

FIREWORKS is a K_S-band selected multiwavelength photometric catalog for the CDF-S region, with matched aperture photometry from imaging in the WFI $U_{38}BVRI$, ACS $B_{435}V_{606}i_{775}z_{850}$, ISAAC JHK_S, all four IRAC channels, and MIPS 24 μm bands (Wuyts et al. 2008). The catalog depth in the K_S band is 24.3 mag (AB), and it covers an area of 138 arcmin^2, overlapping considerably, but not completely, with the CANDELS GOODS-S footprint. The eastern and western edges of the ERS2 strip and a sizable wedge in the NE corner are not included in FIREWORKS, primarily because the WFC3 coverage is wider, in the EW direction, than both the GOODS-S ACS and ISAAC NIR imaging.

For the full multiwavelength catalog, as well as details of the PSF matching, astrometric registration, and photometry used to construct the catalog, we refer the reader to Wuyts et al. (2008). The FIREWORKS catalog includes photometric redshift estimates for all sources, estimated with the EAZY software package (Brammer et al. 2008). The catalog is supplemented with spectroscopic redshifts from numerous efforts in the GOODS-S field. The photometric redshifts are highly accurate, with a median offset in $(z_{\rm spec} - z_{\rm phot})/(1 + z_{\rm spec})$ of 0.001, with an rms scatter of 0.032, increasing to 0.05 at $z \sim 3$. Only a few percent of objects have catastrophic redshift errors. In this work, we employ both photometric and spectroscopic redshifts from the FIREWORKS database, using the former only when the latter is unavailable. For AGNs, we also included spectroscopic redshifts from more recent campaigns available in the literature (Silverman et al. 2010). In addition to redshifts, we adopt stellar mass estimates for galaxies based on FIREWORKS photometry and redshifts.

2.3. Chandra 4 Ms X-Ray Catalog

The CDF-S 4 Ms data set consists of 54 separate exposures from the Advanced CCD Imaging Spectrometer imaging array (ACIS-I) taken between 1999 October and 2010 July as an archival resource for the community. The imaging covers an area of 464 arcmin^2 centered on $\alpha_{J2000} = 03{:}32{:}28.1$, $\delta_{J2000} = -27{:}48{:}26.0$, overlapping with the GOODS-S survey field. We reduced the CDF-S archival data set and extracted a point-source catalog from the combined image. The methods used in the reduction and creation of the catalog, including the determination of PSFs, source detection, and photometry, mirror those developed for the AEGIS-X survey (Laird et al. 2009). The catalog consists of 571 sources with on-axis limiting depths of 10^{-17} erg s^{-1} in the soft (0.5–2 keV) band and 1.9×10^{-17} erg s^{-1} in the hard (0.5–2 keV) band.

3. X-RAY SOURCES IN CANDELS/GOODS-S FIELD

3.1. Near-IR Counterparts of the X-Ray Sources

The ACIS-I PSF varies with location on the detector and can be as large as 8″ (50% encircled energy diameter) at large off-axis angles, which reduces both the spatial resolution and sensitivity to point sources for sources near the edges of the detector. This axis-dependent resolution has to be taken into account when matching X-ray sources to NIR counterparts in the FIREWORKS catalog. To do this, we adopt a Bayesian cross-matching algorithm, which takes into account the positional uncertainty of the X-ray source (which is a function of the X-ray PSF and the presence of any nearby sources), the offset of possible counterparts, and the likelihood of a chance alignment, based on the mean number densities of sources at the *K*-band magnitudes of the possible counterparts. We also visually examined and verified all the cross-matches on the CANDELS *H*-band images, as well as removed any objects with bad imaging data.

Of the 571 X-ray sources in the 4 Ms point-source catalog, 304 lie in the area of the field overlapped by the FIREWORKS catalog, the GOODS-S, and CANDELS imaging. 253 sources (83%) are reliably matched to FIREWORKS counterparts, highlighting the efficiency at which NIR imaging yields good counterparts to X-ray sources. This is because a substantial fraction of sources in deep X-ray catalogs are at redshifts greater than 1.5, which makes them increasing faint to optical imaging surveys, but are easily detectable in NIR bands. Of the remaining 51 sources not matched to FIREWORKS counterparts, a major fraction appear to be associated with large bright galaxies or bright stars. A small fraction appear to be associated with faint sources in the *H*-band images that have no FIREWORKS counterparts. These are good candidates for high-redshift X-ray sources but are beyond the scope of this work.

For the AGNs, standard photometric redshift techniques, such as those in EAZY, can yield results that are systematically in error (Salvato et al. 2009; Luo et al. 2010), due to contamination from the active nucleus. In the CDF-S, Luo et al. (2010) determine redshifts for 2 Ms X-ray point sources using a set of templates specially designed for the AGN population. We compared redshifts for sources from Luo et al. (2010) with matching FIREWORKS counterparts to 4 Ms sources.

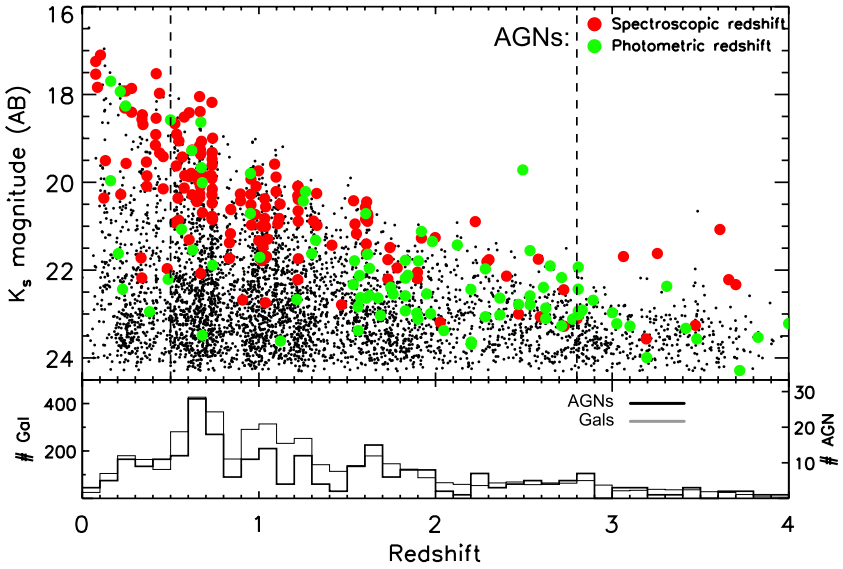

Figure 1. Apparent K_s magnitude plotted against redshift for X-ray sources detected in the CDF-S 4 Ms data set (large points), as well as normal X-ray undetected galaxies from the FIREWORKS catalog (small points). The red points are X-ray sources with a counterpart with a spectroscopic redshift, while the green points are sources with a photometric redshift. The histograms in the lower panel plot the redshift distribution of the FIREWORKS galaxies (thin line, left *Y*-axis) and the AGNs (thick line, right *Y*-axis). The dashed lines mark the redshift range to which we restrict this study ($0.5 < z < 2.8$).

(A color version of this figure is available in the online journal.)

For objects where the redshifts differed by more than 0.05, we adopted the Luo et al. (2010) redshifts and recalculated stellar masses using the FIREWORKS machinery.

In Figure 1, we plot the FIREWORKS K_s magnitude of the cross-matched X-ray sources as a function of redshift and compare them to the distribution of all galaxies in the FIREWORKS catalog. X-ray sources tend to be among the brightest objects at any given redshift. This implies that X-ray AGNs are generally found in hosts that are luminous and relatively massive, as shown in many previous studies (e.g., Nandra et al. 2007; Brusa et al. 2009).

At $z < 1.5$, the majority of X-ray source counterparts have redshifts that are determined through spectroscopic methods and are highly reliable. An increasingly larger fraction of sources at $z > 1.5$ have photometric redshifts. Given the low error and failure rate of FIREWORKS photometric redshifts, this fact should not introduce any significant systematic biases in the spectral energy distribution (SED) fits or color trends (we test this in Section 6.2). For our purposes, we treat both spectroscopic and photometric redshifts equivalently in the following discussions.

For this study, we restrict ourselves to galaxies with redshifts between 0.5 and 2.8, indicated in Figure 1 with dashed vertical lines. The low end of this range marks the redshift at which a substantial fraction of X-ray emission may arise from star formation or weak AGN activity ($L_{2-10} < 10^{42}$ erg s^{-1}). The upper end is the redshift at which the rest-frame 4000 Å break enters the observed *H* band (the reddest band we consider for aperture photometry). By applying an upper redshift cut, we restrict our sample to redshifts at which the *H* band traces light from the bulk of a galaxy's stars. Our redshift cut yields a working sample of 176 X-ray sources.

3.2. X-Ray Luminosities and Nuclear Obscuration

The multi-band X-ray count rates and FIREWORKS redshifts are used to estimate rest-frame X-ray luminosities and obscuration in the X-ray sources. We assume that all sources have an intrinsic power-law spectrum at X-ray wavelengths with a photon index of $\Gamma = 1.9$ (Nandra & Pounds 1994). We simultaneously fit the fluxes in the observed-frame full (0.5–10 keV), soft (0.5–2 keV), hard (2–10 keV), and ultra-hard (4–10 keV) X-ray bands, corrected for Galactic absorption, to estimate the intervening hydrogen column density ($N_{\rm H}$), using the photoelectric cross sections of Morrison & McCammon (1983). These fits are used to derive intrinsic (de-absorbed) hard X-ray luminosities L_{2-10} in the rest-frame 2–10 keV band.

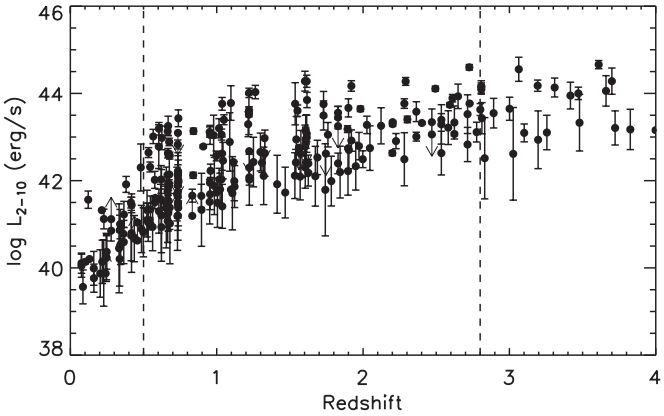

Figure 2. Rest-frame X-ray luminosity in the hard band (2–10 keV) vs. redshift of CDF-S X-ray sources with FIREWORKS counterparts. The dashed lines mark the redshift range to which we restrict this study ($0.5 < z < 2.8$).

In Figure 2, we plot L_{2-10} against redshift for our sample. Nine sources had $N_{\rm H}$ estimates that were greater/lesser than the upper/lower allowed bound ($\log N_{\rm H} = 25/19$ cm^{-2}), typically because they are detected in only a single X-ray band. We removed these sources from our sample. Galaxies with $L_{2-10} < 10^{42}$ erg s^{-1} can possibly be contaminated by X-ray emission from star formation and stellar remnants (Bauer et al. 2002). Therefore, we set this luminosity limit as a minimum criterion for an X-ray source to be a pure AGN. The application of these two criteria excludes 58 objects, leaving us with a final working sample of 118 bona fide AGNs spanning a redshift range of 0.5–2.8 and almost three orders of magnitude in X-ray luminosity.

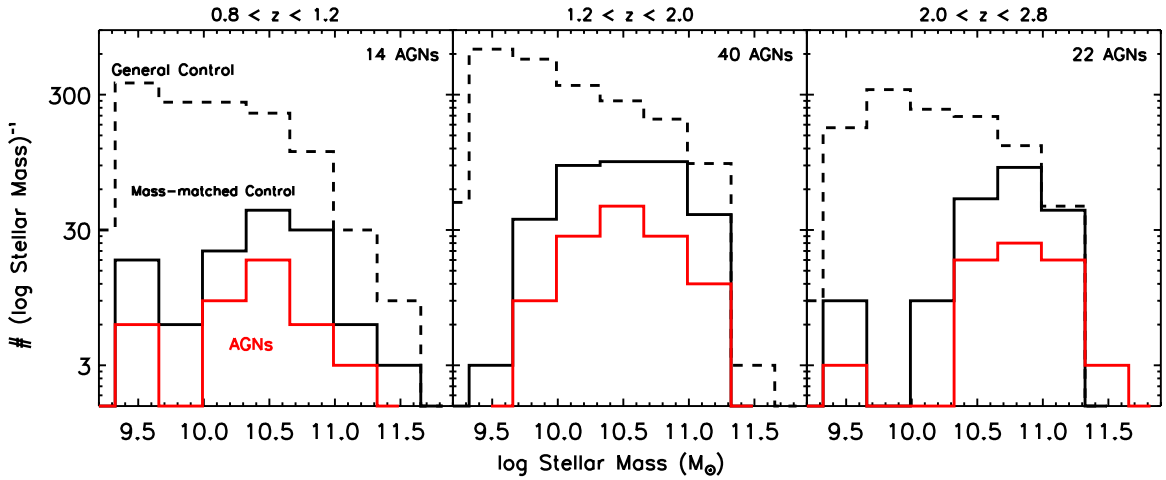

Figure 3. Stellar mass (M_*) distributions of AGNs (red solid lines) compared to the general control sample (dashed lines) and the mass-matched control sample (black solid lines) in three redshift bins. The AGNs (and mass-matched control galaxies) tend to be more massive than the field galaxy population.
(A color version of this figure is available in the online journal.)

The de-absorbed X-ray luminosity is generally quite robust to the exact parameters of the X-ray fits, since for most of our redshift range, the rest-frame 2–10 keV band is bracketed by the soft and hard bands in the observed frame. In addition, the optical depth to photoelectric absorption in the hard band is low for typical obscuring columns in X-ray selected AGNs. However, the value of $N_{\rm H}$ is generally more uncertain and has systematic variations with redshift, as the obscuration-sensitive rest-frame soft band is redshifted out of the Chandra/ACIS bandpass. In particular, higher redshift AGNs will have systematically higher $N_{\rm H}$.

3.3. Control Sample

The main goal of this work is to explore the nature of the host galaxies of AGNs at high redshifts. In order to fully understand AGN hosts, they must be placed within the context of the normal field galaxy population at comparable epochs. Many studies have shown that there has been substantial evolution in the properties of normal galaxies since $z \sim 3$: the star formation rate at a given stellar mass has decreased by an order of magnitude (Noeske et al. 2007; Tresse et al. 2007), the space density and stellar mass of red galaxies have increased by a similar amount (Arnouts et al. 2007; Taylor et al. 2009), and stellar mass functions of galaxies show considerable evolution, especially at the low-mass end (Marchesini et al. 2009). In addition, these studies also demonstrate considerable correlation of galaxy properties with stellar mass. We control for these transformations and variations by defining two sets of normal galaxies, to which we compare the properties of AGNs throughout this paper. The first set is a representative sample of inactive galaxies with masses and luminosities comparable to the AGNs. The second is a refined sample with a stellar mass distribution that is matched to the AGNs.

First, we examined the images of all FIREWORKS galaxies without X-ray detections in the redshift range $0.5 < z < 2.8$ that occupy the same range in absolute B-band magnitude and stellar mass as the AGNs ($\log M_* > 9.3\ M_\odot$ and $M_B < -19.5$). We excluded any that did not have images in the WFC3 J/H bands and the four GOODS ACS bands, as well as a few that lay too close to the edges of the ACS and WFC3 mosaics, or those with image defects or contamination from bright nearby stars or galaxies. This left us with a high-quality set of 1683 inactive galaxies with a similar range of luminosity, mass, and multiwavelength coverage as the AGNs in our sample. The redshift distribution of these galaxies, hereafter called the "general control sample," is similar to that of the AGNs (lower panel of Figure 1).

From the general control sample, we applied a further selection to get a "mass-matched control sample." First, we divided the AGNs and normal galaxies by redshift into the same redshift bins as those used in our subsequent comparative study (see later sections). For each AGN in a bin, we randomly chose three distinct normal galaxies in the same redshift bin with a stellar mass within 0.2 dex of the AGN's mass. This tolerance is a balance between a statistically large sample of control galaxies and the need to closely match the mass distribution of the AGNs, especially at high masses, at which the AGN fraction among galaxies can be quite large at $z \sim 2$.

At intermediate to high AGN luminosities, contamination of optical and IR light by the emission from the active nucleus can systematically alter stellar mass estimates for AGN hosts. In the next section, we outline a method to exclude AGNs with the strongest contamination, using a combination of X-ray luminosity and obscuration cuts. These cuts only affect a small fraction of objects (9%). For most AGNs in our sample, the effects of contamination are minimal and do not significantly bias our control sample selections.

In Figure 3, we compare the stellar mass distributions of the two control samples with the AGNs in three redshift bins: 0.8–1.2, 1.2–2.0, and 2.0–2.8. These three bins will be used frequently in the rest of this work and, for brevity, are termed the "low," "intermediate," and "high" bins, respectively.

The general control sample has a mass distribution (dashed line) that is approximately Schecter-like, while that of the AGNs and mass-matched control sample (red and black solid lines) drop off strongly toward low masses. Note the close correspondence between the latter two distributions, which highlights the quality of our mass-matching procedure.

AGNs are weighted toward being found in rather massive galaxies. The peak in the AGN mass distribution is at $\log M_* \approx$ 10.5–10.7, increasing slightly with redshift. In addition, the fraction of massive galaxies hosting AGNs increases drastically with redshift. While AGNs are only a few percent of similar-mass galaxies in the low bin, the fraction increases to more than 30% at the high-mass end in the high bin. The typical stellar masses of the AGN hosts are much higher than the

mass incompleteness limit of the FIREWORKS catalog at all redshifts. This implies that the slight evolution in the peak mass is probably real and not a consequence of differences in the AGN luminosity range with redshift. It may be related to the strong increase in the space density of AGNs. A detailed look at mass functions of AGNs is beyond the scope of this paper, but we discuss some aspects of the evolution of the AGN mass function in Section 10.

4. APERTURE PHOTOMETRY

For each galaxy in our AGNs and control samples, we performed aperture photometry on the full set of seven *HST* images from four ACS/GOODS and two to three WFC3/CANDELS bands. We first used the PSFMATCH routine within IRAF[10] to develop convolution kernels to match the PSFs of the images in all bands to those of the *H* band. The PSF-matching procedure reproduces the extended structure of the *H*-band PSF very accurately in all the GOODS and WFC3 images. However, the simulated PSFs had slightly broader cores than that in the *H* band (by 15%–20%, depending on the width of the original PSF), a result of the apodizing filter applied to the convolution kernels to remove high-frequency noise in the original PSFs. Photometry of galaxies in apertures close in size to that of the WFC3 *H*-band PSF (such as the "nuclear" aperture used in later sections) yields SEDs that are too red, as some of the light in the core of the bluer bands is scattered out of the aperture by the PSF-matching process. The degree to which this effect operates is a strong function of the compactness of the galaxy image. Figure 4 illustrates how differences in the shape of simulated PSFs affect the photometry of galaxies. We convolved a suite of circular Sérsic model galaxies (described in the Appendix) with two PSFs: the drizzled TinyTim *H*-band PSF and the ACS *B*-band PSF matched to that of the *H* band using our PSFMATCH kernels. The *B* band was chosen for this illustration since its PSF differs the most from the *H*-band PSF. In the figure, we plot the fractional difference between the flux of a model galaxy convolved by the two PSFs as a function of the Sérsic index of the model. The two panels represent two sets of simulated galaxies with very small and relatively large $R_{\rm eff}$.

In general, imperfect PSF matching leads to larger differences in the nuclear aperture (as much as 14%) but rather negligible effects in the default outer aperture (<5%, but only for high Sérsic galaxies). This holds for both the most compact and fairly large galaxies. Clearly, the artificial "PSF-reddening" will not affect the results of our extended-light photometry (Section 7) but may play a role in the interpretation of color gradients (Section 8), as discussed in that section.

After convolving the images in each band to bring them to a common PSF, we used the IDL program APER to measure counts in a set of annular apertures, ranging from 0.″1 to 4″, centered on the coordinates of the *H*-band centroid. The photometric measurements were converted to AB magnitudes using zero-points taken from GOODS v2.0 (Giavalisco et al. 2004) and STScI WFC3 documentation. Errors were estimated from the multidrizzle weight maps, with a standard correction for correlated pixel-to-pixel noise.

[10] Image Reduction and Analysis Facility, distributed by the National Optical Astronomy Observatory.

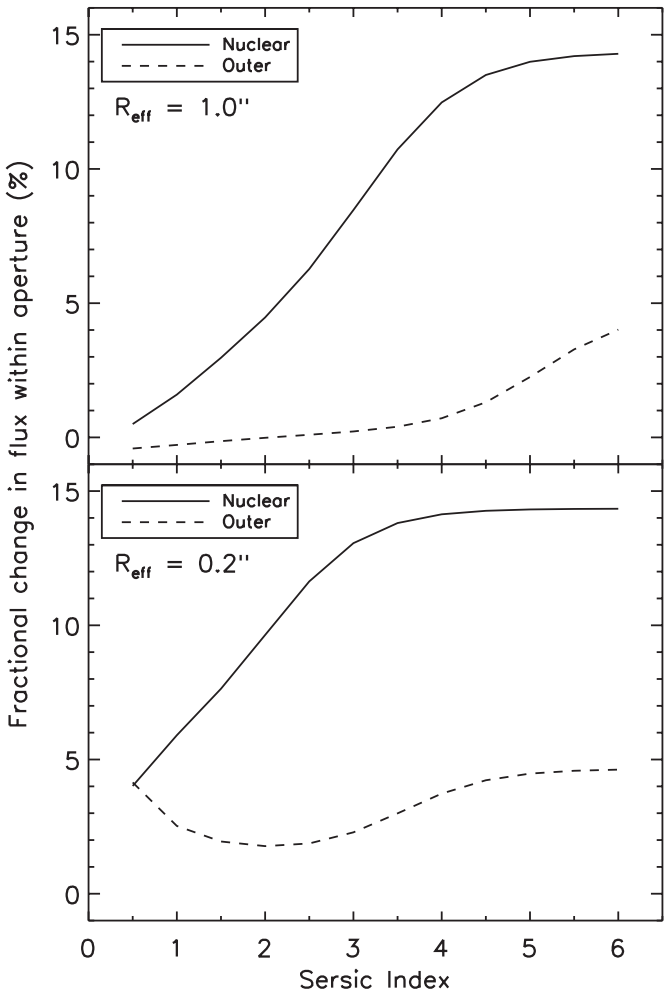

Figure 4. Absolute fractional difference between the flux in simulated galaxies convolved by two different models of the CANDELS/*H*-band PSF, as a function of the original Sérsic index of the simulated galaxy. The two model PSFs are the drizzled TinyTim CANDELS-Deep PSF, an accurate model of the actual PSF, and a GOODS/ACS *B*-band PSF, matched to the *H* band using PSFMATCH kernels. The fluxes are measured in two apertures: a nuclear aperture with a radius of 0.″1 and an annular "outer" aperture of radius 0.″4–1″. The difference between the fluxes is expressed as a fraction of the flux in the aperture from the CANDELS-Deep PSF convolved image. The panels show results for two sets of simulated galaxies with different $R_{\rm eff}$: very compact galaxies in the lower panel and relatively large galaxies in the upper panel. The nuclear aperture is affected considerably by light scattered from the core by imperfections in our PSF-matching procedure, but the outer aperture is only marginally affected by scattered light (<5%).

5. MODEL FITS AND STATISTICS

5.1. SED Fitting and Parameter Estimation

The main thrust of this paper is to self-consistently study rest-frame properties (colors, mean extinctions) and the stellar populations (ages, star formation histories) of X-ray selected AGN hosts across redshift and compare them to the properties of inactive galaxies. Toward these ends, we employ a library of synthetic SEDs derived from the population synthesis models of Maraston (2005). Starting with a set of single stellar populations (SSPs) with metallicities of 1/2, 1, and 2 times solar, we generated models with three possible SFHs: constant star formation, exponentially decaying star formation (negative "τ-models"), and exponentially *increasing* star formation (positive "τ-models"). The latter set of models are rarely employed in studies to date, but recent

work suggests that SFHs that increase with time may be more relevant at $z \gtrsim 2$, since the mean star formation rate density of the universe turns over at that epoch (Maraston et al. 2010). The SFH is parameterized by a finely sampled set of 43 ages (since the onset of star formation), ranging from 0.01 to 15 Gyr, and 16 exponential timescales (τ), ranging from 0.05 to 20 Gyr. In addition, we applied a foreground-screen dust reddening prescription with a Calzetti reddening law (Calzetti et al. 1994), parameterized by the visual extinction A_V in 16 uniformly logarithmic steps from 0.001 to 7. We derived model magnitudes for each SED at a set of redshifts between 0.4 and 4.0, with uniform steps in redshift of 0.01. At any redshift, only models that were younger than the age of the universe were considered. Magnitudes were evaluated in the observed frame for the seven *HST* bands, ISAAC K_S, and the four IRAC bands, using the most up-to-date filter functions publicly available. Our library of model SEDs is sufficient to capture the bulk of spectral variation among galaxies, verified by comparing the empirical range of rest-frame colors among galaxies in the FIREWORKS catalog with that of our model set.

There is some debate in the literature about the relative importance of thermally pulsating asymptotic giant branch stars on the determination of stellar populations in galaxies (Maraston et al. 2006; Kriek et al. 2010; Pforr et al. 2012). Our choice of SSP models allows a strong contribution from this transient population, while other popular models, such as those of Bruzual & Charlot (2003), do not. Analysis of real galaxy samples shows that the choice of model library can contribute to much of the systematic differences found among studies (Kannappan & Gawiser 2007; Muzzin et al. 2009), as well as different choices of SSP parameters such as the choice of mean metallicity, extinction law, and the shape and turnover of the initial mass function (Conroy et al. 2009; Pforr et al. 2012). Since we use the same modeling methodology to fit all our galaxies, comparisons between different samples should be internally consistent, though a comparison to other studies with a different choice of synthesis models will likely show systematic differences in derived SFH parameters at the factor of 2–3 level (Muzzin et al. 2009). $U - V$ colors are unaffected by the choice of model library.

For each galaxy and a given annular aperture, we fit for a scaling parameter that minimized the χ^2 difference between the model and measured fluxes, at a grid redshift closest to the measured redshift of the galaxy. This minimum χ^2 for the model was then stored. In this way, we obtained a four-dimensional χ^2 space for each galaxy, parameterized by SFH model (constant/range of positive and negative τ), age, A_V, and metallicity. We applied an additional constraint that the synthesized K_S and IRAC magnitudes for any model fit to the SED of an annular aperture must be less than the total measured K_S and IRAC magnitudes of the galaxy, up to a rest-frame wavelength of 1.6 μm. In practice, this constraint only excludes the most dusty models at the highest redshifts, but it is included for physical consistency.

From this χ^2 space, we developed a method to derive the best-fit value and accurate confidence intervals for any model-dependent parameter (age, *tau*, rest-frame colors, A_V), similar to the procedure described in Salim et al. (2005) for population fits to galaxies from UV-to-IR SEDs. Consider, as an example, the rest-frame $U - B$ color of the galaxy. We concentrate on this color since it is uniquely sensitive to the mean light-weighted stellar population of a galaxy, since the two bands constituting the color lie on either side of the 4000 Å break. Each model has a particular value of rest-frame $U - B$, calculated directly from its synthetic spectrum. The best-fit value of $U - B$ corresponds to the model with the lowest χ^2 value. The uncertainty in $U - B$ is given by the minimum and maximum color of all models that deviate from the lowest χ^2 by less than 3.5, which defines the appropriate 68% (1σ) confidence interval for three degrees of freedom (seven bands—four model parameters). The advantage of using the full χ^2 space is that systematic uncertainties due to degeneracies in the model space, which can frequently be larger than purely statistical uncertainties, are taken into account in this method.

In this way, we arrive at best-fit values and confidence intervals for observed and intrinsic rest-frame colors, visual extinction, stellar age, τ, and the ratio of stellar age over τ (the "normalized age") for each galaxy. The last two quantities are only appropriate for galaxies fit with τ models. Note that systematic differences may be expected in the best-fit values of SFH parameters depending on the choice of synthesis library. A detailed treatment of these systematics is beyond the scope of this work. However, since we use the same library for all our fits, comparisons between AGNs and control galaxies should be internally consistent.

5.2. Monte Carlo Bootstrapped Distributions

A important part of the following analysis involves comparing distributions of various estimated quantities (colors, SFH parameters) between AGNs and inactive control galaxies. The small size of the sample and the large uncertainties on some of the parameters from the SED fitting analysis make interpretation of any differences in the distributions of best-fit parameters rather difficult. As the library of models does not uniformly sample parameter space, best-fit values of a parameter can be overrepresented in regions of parameter space that are more well sampled than others.

To enable a reasonable comparison to be made between the parameter distributions of AGNs and control galaxies, we developed a two-step Monte Carlo bootstrap approach to arrive at more representative distributions for both samples. For each object, we take the best-fit parameter from the SED fits to be a median value. We randomly vary the parameter about this value, taking the upper and lower 1σ confidence intervals as the standard deviations of a two-sided piece-wise Gaussian probability distribution, where the probability of a random deviate being positive or negative is 0.5 (by construction, as the best-fit value is assumed to be a median value). For some parameters, such as stellar age, we apply upper and lower bounds to the random deviate consistent with any limits enforced in the SED fitting process. This process is repeated 1000 times per object. The final distribution in each redshift bin is derived from the entire simulated set of parameters for all objects (AGNs or control) in that bin. We term this bootstrapping step "Loop 1." While Loop 1 takes into account the uncertainties that come out of the SED fitting process, it does not consider the effects of the limited sample size of the AGNs—stochastic effects can play a big role in the shape of a parameter distribution. To account for this, we run Loop 1 on a subsample of N randomly chosen galaxies from the control sample in a redshift bin, where N is the number of AGNs in the same redshift bin. This second set of Monte Carlo simulations is called "Loop 2," and it allows us to place upper and lower 1σ uncertainties on the distribution of the control galaxies resulting from stochastic effects from the small size of the AGN sample in any given bin. The distributions

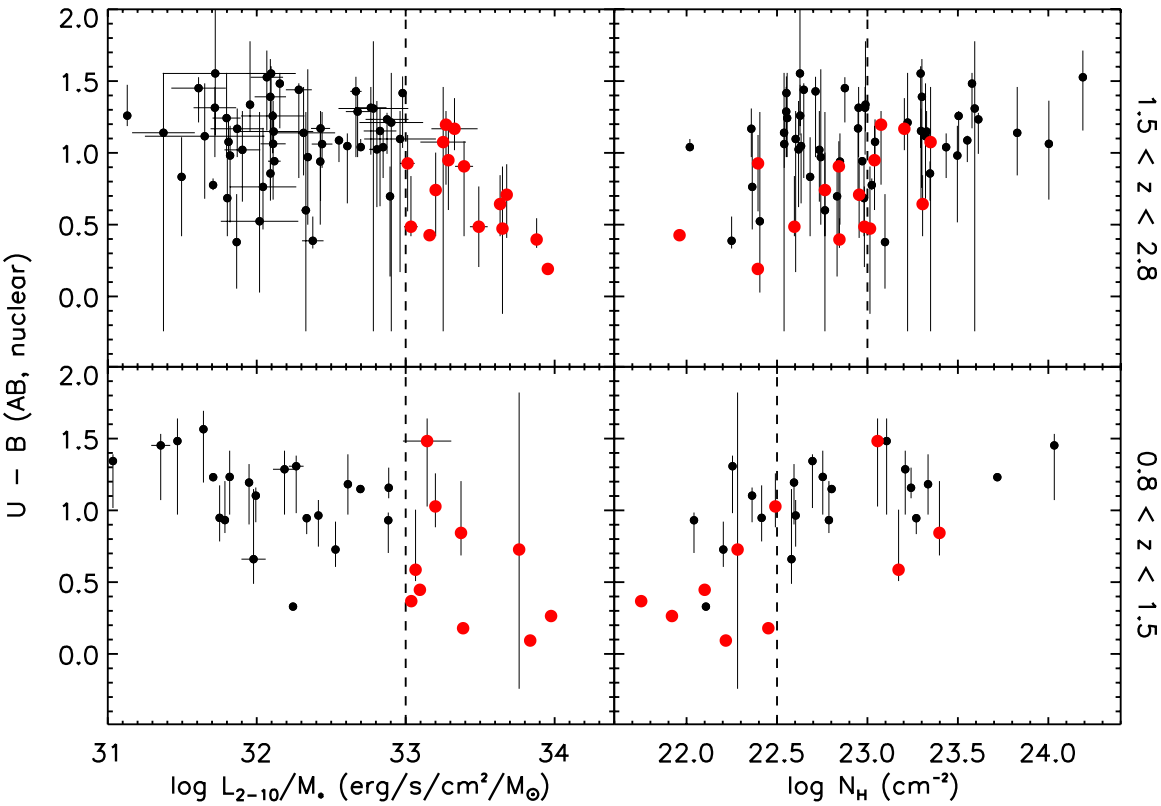

Figure 5. Rest-frame nuclear $U-B$ colors of AGN hosts plotted against the ratio of hard-band X-ray luminosity to stellar mass (left panels) and the hydrogen column density of X-ray obscuring gas $N_{\rm H}$ (right panels). The lower panels show AGNs at intermediate redshifts ($0.8 < z < 1.5$), while the upper panels show AGNs at high redshifts ($1.5 < z < 2.8$). The vertical dotted line in the left panels marks the transition value of L_{2-10}/M_* beyond which nuclear emission from the AGN prominently affects the nuclear colors. These sources are marked as red points in all panels and appear to separate out in the plane of color vs. $N_{\rm H}$. The blue sources are generally soft, while the red sources are typically harder, with high values of $N_{\rm H}$. The dashed vertical lines in the right panels mark the values of $N_{\rm H}$ used in combination with the transition L_{2-10}/M_* to separate out sources with nuclear contamination.

(A color version of this figure is available in the online journal.)

of AGNs and control galaxies are only significantly different if they have consistent offsets that are larger than the 1σ errors bars on the control galaxy distributions. Note, however, that this process does not regularize stochastic variations due to the limited sample size of the control galaxies. In all redshift bins, the mass-matched control galaxy samples range between 45 and 110 objects, and the general control sample, of course, is much larger. Therefore, stochastic effects among these galaxies should be small. However, we have checked the validity of our main results through several iterations of the mass-matching procedure described in Section 3.3. All our conclusions are essentially unchanged in several randomly different mass-matched control samples.

6. NUCLEAR COLORS AND OBSCURATION

The active nucleus is a source of considerable high-energy radiation. In cases where the emission from the AGN is relatively unobscured to optical light, the nucleus can appear as a point source in galaxy images, frequently blue in color. Bright unobscured nuclear point sources can influence the integrated colors of AGNs and, quite drastically, the apparent morphology of AGN hosts (Pierce et al. 2010a). The high spatial resolution of the WFC3 NIR images allows a better characterization of the SED of the nuclear light in AGNs at $z \sim 1$ and allows us to constrain the contribution of non-stellar emission to the nuclear light in AGNs at $z \sim 2$ more accurately than ever before.

The relative degree to which light from an unobscured active nucleus can contaminate the light of a galaxy is related directly to the luminosity of the AGN and inversely to the stellar luminosity of the galaxy. To account for both dependencies, we construct a parameter L_{2-10}/M_*, which is the ratio of the X-ray luminosity of an AGN to this stellar mass of its host.

In Figure 5, we plot the rest-frame "nuclear" $U-B$ color of the X-ray AGNs against L_{2-10}/M_* (left panels) and the X-ray obscuring hydrogen column density $N_{\rm H}$ (right panels). The "nuclear" photometry is estimated within a central circular aperture 0.″2 in diameter, corresponding to a physical scale of ≈1 kpc across our redshift range of interest. The aperture size is larger than the 0.″15 FWHM of the WFC3 H-band PSF and encloses ≈40% of any unresolved central light. We separate the AGNs into two redshift bins in this plot: $0.8 < z < 1.5$ and $1.5 < z < 2.8$.

The nuclear colors of AGNs at $0.8 < z < 1.5$ are predominantly redder than $U - B = 0.8$ (approximately the top of the Blue Cloud at these redshifts; see Section 7.3.1). However, above a transition value of $\log L_{2-10}/M_* = 33$ erg s^{-1} $M_\odot^{-1}$ (red points), some AGNs show scatter toward much bluer nuclear colors. In addition, the blue color appears to correlate with L_{2-10}/M_*, suggesting that the excess blue light in the centers of these AGNs comes from nuclear emission. Indeed, a visual inspection of these bright AGNs with blue nuclei clearly shows nuclear point sources (Figure 6). Most also have broad AGN lines visible in their spectra (Szokoly et al. 2004).

The right panels of Figure 5 allow us to compare the X-ray obscuration properties of the AGNs as a function of nuclear color. In the lower right panel, the red and blue branches of the bright AGNs (red points) separate out in $N_{\rm H}$. Objects with

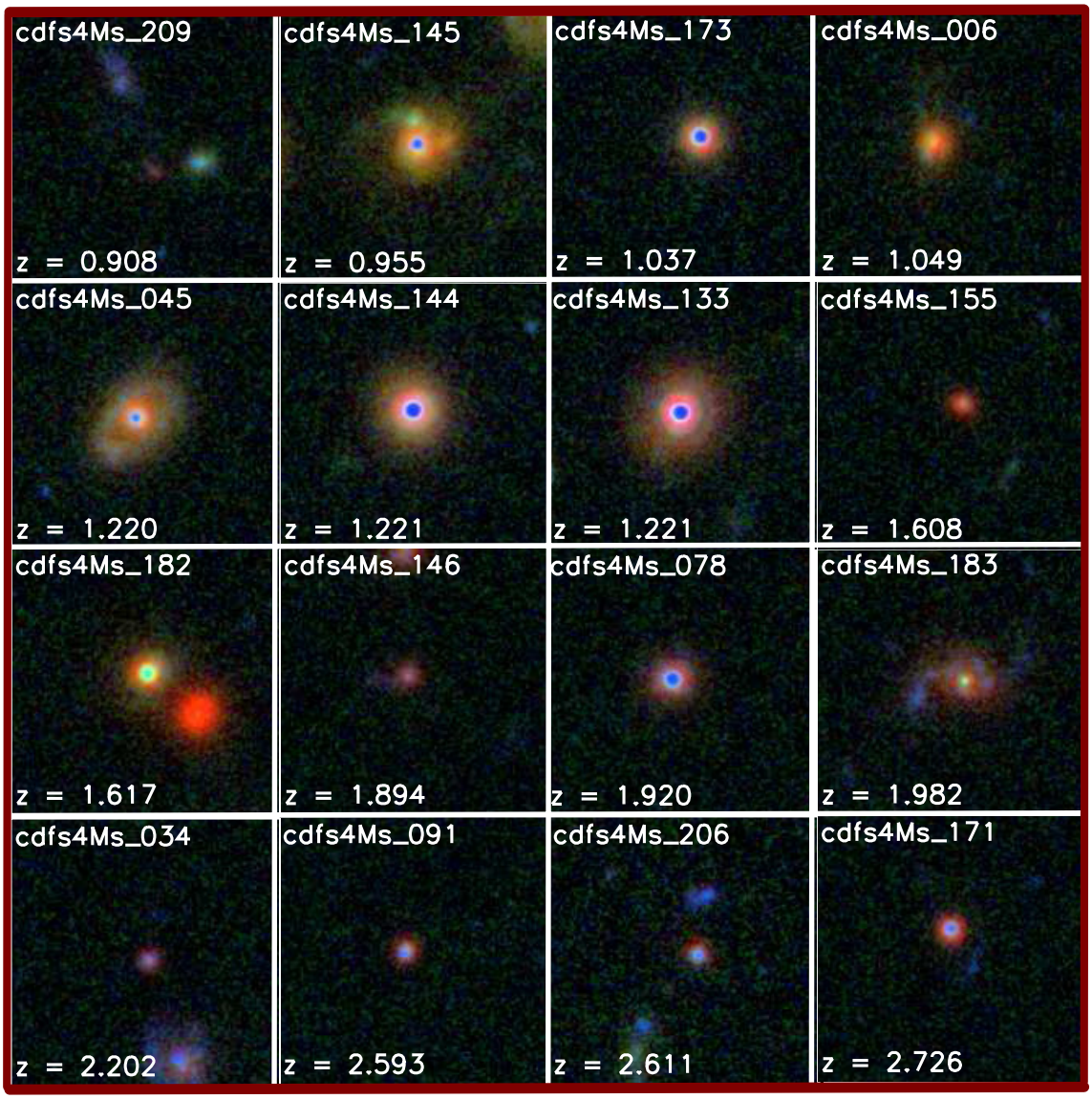

Figure 6. Three-color VzH images of the 16 AGNs in the redshift range $0.8 < z < 2.8$ that have been flagged as galaxies with strong nuclear AGN contamination, based on X-ray based criteria (Section 6). Bright blue nuclear point sources are seen in almost all these sources.

(A color version of this figure is available in the online journal.)

blue colors all show relatively low obscuration ($\log N_{\rm H} \sim 22$), while those with red colors show a larger range in $N_{\rm H}$ but tend to be higher. In other words, luminous AGNs that are unobscured toward the nucleus in optical light are also relatively unobscured at X-ray wavelengths, while those that are obscured at optical wavelengths generally show a larger X-ray obscuration as well.

The anti-correlation between visible nuclear optical emission and the level of X-ray obscuration has been noted in previous work on AGN host color gradients, typically at $z \sim 1$ (Pierce et al. 2010b). The simplest interpretation of this trend is the existence of a relationship between the medium that obscures the optical light of the AGN accretion disk and the medium that obscures the X-ray emission.

A similar behavior is seen at high redshifts (top left and right panels), with some qualitative differences. The colors of the unobscured AGNs are not as blue as at lower redshifts. This could be because the optical obscuration toward the nucleus at $z \sim 2$ is larger on average compared to that at $z \sim 1$, since the gas fraction of galaxies increases toward high redshifts. Another possibility is that the fraction of stellar light within the nuclear aperture is larger at $z \sim 2$, as galaxies at these redshifts are generally quite compact. This will reduce the contrast of AGN emission against that of the galaxy.

In addition, the mean $N_{\rm H}$ between the AGNs with blue and red nuclear colors is not as pronounced at $z \sim 2$ as at intermediate redshifts. This difference is hard to interpret accurately, since the X-ray spectral fit parameters, and especially $N_{\rm H}$, can vary systematically with redshift. If true, it may represent a gradual change in the relationship between optical and X-ray obscuration toward higher redshifts. For example, at $z \sim 1$ optical obscuration could come primarily from dusty gas in the vicinity of the SMBH, such as the putative dusty torus that is invoked in Unification schemes for local AGNs (Antonucci 1993). However, at $z \sim 2$, more of the optical obscuration may arise from intervening dust within the gas-rich interstellar medium of the host galaxy. In both cases, most of the X-ray obscuration probably arises in very dense gas surrounding the

AGN accretion disk, since the typical gas mass surface densities of galaxy disks generally cannot account for the high values of $N_{\rm H}$ (e.g., Kennicutt & Evans 2012).

We are now able to decide on criteria to allow us to flag and remove AGNs with likely strong nuclear point sources from the following analysis of outer colors and SFHs. Since nuclear colors can be blue due to both AGN emission and strong star formation, we choose not to use pure color criteria, since this can remove galaxies with genuine nuclear star formation, rather than strong AGN activity. Instead, we employ purely X-ray based criteria. We decide on $\log L_{2-10}/M_* = 33$ erg s^{-1} $M_\odot^{-1}$ and $\log N_{\rm H} < 22.5/22.9$ cm^{-2} at z lesser/greater than 1.5, guided by the results of Figure 5.

7. HOST GALAXY COLORS

In this section, we study the rest-frame $U-B$ color of the AGN hosts in annular apertures that are relatively free of nuclear contamination and compare them to the rest-frame $U-B$ color of various control galaxy samples across various redshift bins.

7.1. Choice of Working Annulus

In this study of extended light, we will work in an annular aperture of fixed angular size across all redshifts. This is preferred over working with apertures of fixed physical size for two primary reasons:

1. Any comparison of photometric properties between annular apertures of different sizes will need to take into account the smearing effects of the PSF, which is dependent on the light profile of the galaxy, the strength of nuclear AGN emission, and the radius of the annular aperture. These effects can be hard to model a priori and may have considerable uncertainties and systematics. However, working in fixed annular apertures at all bands and redshifts keeps these effects fixed as well and greatly simplifies the interpretation of any comparisons.
2. The angular diameter distance scale varies by less than 15% between the redshifts of 0.8 and 3 and only by about 30% between redshifts of 0.5 and 1. Therefore, a comparison of outer colors of galaxies between $z \sim 1$ and $z \sim 2$ at fixed angular apertures is essentially equivalent to a comparison at fixed physical apertures.

To arrive at an optimal annular aperture to study the extended light of AGN hosts, we rely on the measurements of the sizes of AGN hosts (and inactive galaxies) at $z \sim 2$ presented in Schawinski et al. (2011). This work used the two-dimensional profile modeling code GALFIT (Peng et al. 2010) to model the H-band images of high-redshift AGNs (including the effects of central point sources) in the ERS2 field and find that their half-light radii $R_{\rm eff}$ span a typical range from 0.″25 to 0.″75, which corresponds to approximate physical sizes of 2–6 kpc.

For our purposes, we choose an outer annular radius of 1″, which encompasses a substantial fraction of the light of galaxies across our redshift range of interest. The inner radius of the annulus has to be large enough to minimize contamination from the central light of the galaxy (nuclear or stellar), so that valid measure of color gradients can be made. After experimenting with the relative size of the H-band PSF and various aperture sizes using a suite of model AGNs (see the Appendix), we settled on an inner aperture of 0.″4. Beyond this radius, the extended blue light in the smaller galaxies is contaminated by unresolved central emission at the level of a few tens of percent, and even less for the larger galaxies.

Having said this, nuclear continuum emission in bright AGNs can still substantially affect the extended-light aperture at blue and UV wavelengths, which will skew our SED fits toward bluer colors and younger mean ages. Therefore, we also employ the criteria based on our study of nuclear colors to remove the small fraction of AGNs with strong nuclear point sources.

7.2. Context: Field Galaxy Color–Mass Diagrams

Before a detailed study of AGN colors, we set the context by examining the extended-light colors of inactive galaxies through the use of $U-B$ color–mass diagrams (CMD$_*$). In the upper three panels of Figure 7, we plot the CMD$_*$ of galaxies in the three redshift intervals defined earlier: low ($0.8 < z < 1.2$), intermediate ($1.2 < z < 2.0$), and high ($2.0 < z < 2.8$) bins. $U-B$ colors in this figure come from extended-light photometry, which generally differ from integrated colors.

We begin by highlighting the bimodality evident in the outer colors of the non-active control galaxies at all redshifts. A Red Sequence from evolved or reddened galaxies can be easily distinguished in the low- and intermediate-bin panels. A slope to the sequence is discernible, though the data are not sufficient to identify any evolution in the slope. In the high bin, the low-mass end ($\log M_* < 10.5$) of the Red Sequence is diminished, but red galaxies can still be found at high masses.

In addition to the Red Sequence, a cloud of blue, star-forming galaxies is also seen in the CMD$_*$, typically at lower masses than the red galaxies. The density of the Blue Cloud relative to the Red Sequence increases with redshift, while the typical color of the Blue Cloud decreases with redshift: median $U-B$ values for low/intermediate/high bins are 0.7/0.6/0.45 mag. This is primarily due to higher star formation and lower characteristic stellar ages of star-forming galaxies at higher redshifts. Since we deal primarily with AGN host properties in this paper, we refrain from a detailed treatment of the form of the bimodality and its evolution with redshift, noting only that a bimodality exists and is well defined.

We use the CMD$_*$ to evaluate the location of the Green Valley in extended light. Since radial color gradients exist among massive star-forming galaxies (e.g., Guo et al. 2011), we expect the location of the Green Valley in these CMD$_*$ to differ slightly from definitions based on integrated photometry (e.g., Willmer et al. 2006). We therefore define our own Green Valley as the dividing line between the Red Sequence and Blue Cloud, corresponding to the region of minimum density in the CMD$_*$ between these two populations of galaxies. Since the Red Sequence has a definite slope with stellar mass, the Green Valley line will also be sloped. We assume that the slope of the Green Valley in our $U-B$ CMD$_*$ is constant with redshift. We calibrate this slope in the intermediate bin, which has the largest density of galaxies, by varying the line parameters to place it at a minimum in the distribution of $U-B$ offsets from the line. We derive a slope to the Green Valley line of 0.09 mag per dex in M_*. For the other two redshift bins, we kept the slope constant at this value but vary the intercept to identify the Green Valley. The location of the Green Valley is shown in each panel of Figure 7 with solid green lines.

7.3. AGN Hosts versus Inactive Field Galaxies

The upper panels set the context of the field galaxy population within which we couch the CMD$_*$ of the AGN hosts. In the lower three panels of Figure 7, we plot the AGNs as red stars and mass-matched control galaxies as black squares, in addition to the general control sample.

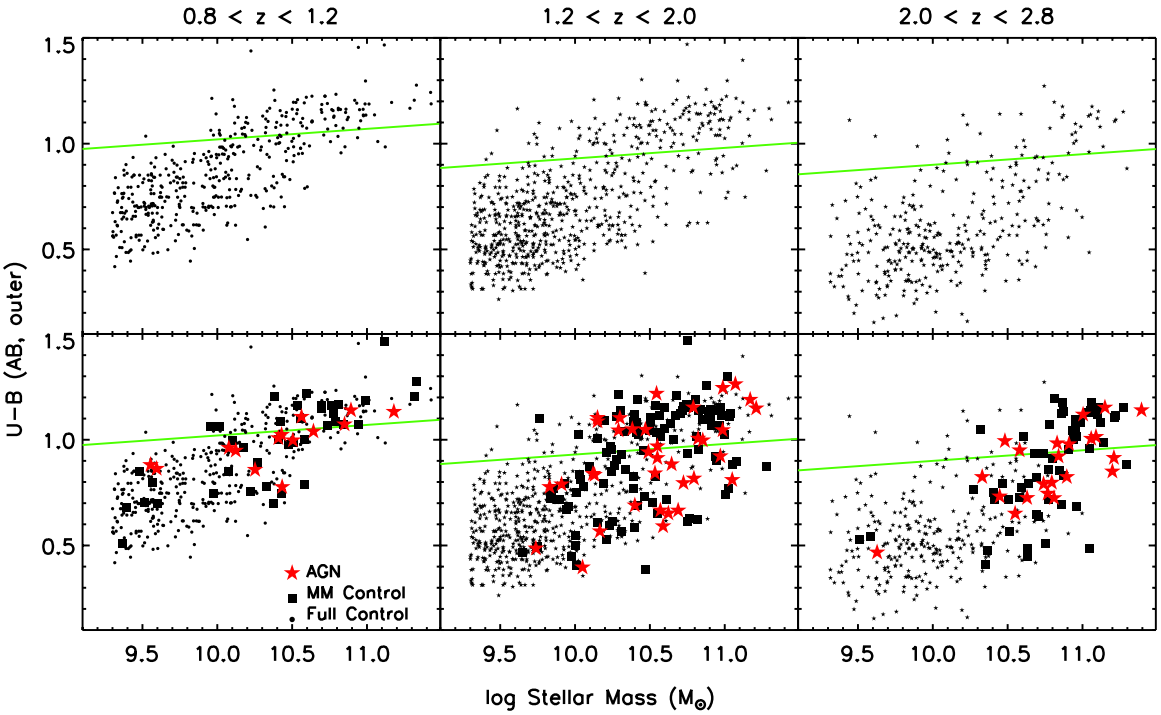

Figure 7. Outer $U-B$ color vs. stellar mass for AGNs and normal galaxies in three redshift bins. In the upper panels, the small points show all galaxies in the FIREWORKS catalog with $\log M_* > 9.3\,M_\odot$ and $M_B < -19.5$ (the general control sample), for which we have performed extended-light photometry. The green lines mark the location of the Green Valley, derived separately in each bin. In the lower panels, in addition to the same small points as in the upper panels, the large points show outer colors for AGNs (red) and mass-matched control galaxies (black). The AGNs tend to have high stellar masses and redder colors than the normal galaxy population.

(A color version of this figure is available in the online journal.)

At all redshifts, the AGNs are distributed differently in the CMD_* as compared to the general control sample. Their stellar masses are typically higher and their colors are typically redder, and they display a flatter distribution of $U-B$ colors with a weaker bimodality. This tendency has been observed in many previous studies of the integrated photometry of AGNs (e.g., Nandra et al. 2007; Cardamone et al. 2010), and we show here, using extended-light photometry, that it is not due to low levels of nuclear blue light pushing red hosts into the Green Valley, but is intrinsic to the stellar populations of the AGN hosts.

A clearer picture of the differences between AGNs and field galaxies comes from their distribution of $U-B$ offsets. The offset is defined as the difference in the $U-B$ color of a galaxy from the Green Valley color at its particular stellar mass, i.e., it is the offset of the galaxy from the Green Valley line defined above. We refer to this offset as $\Delta U-B$.

In the left three panels of Figure 8, we compare the $\Delta U-B$ distributions of AGNs (solid histograms) and the general control sample (solid histograms) in all three redshift bins. These histograms show the best-fit colors determined from the SEDs and have not been "regularized" by the bootstrapping procedure described in Section 5.2. Nevertheless, the difference between the distributions is clear. The general control sample shows a wide range in $\Delta U-B$, with a peak at a negative (blue) value that decreases with redshift. The AGNs, on the other hand, display a narrower distribution that peaks at significantly redder colors, more or less around the Green Valley ($\Delta U-B=0$). The distribution of AGN colors is narrowest in the low bin and gets progressively broader in the two higher redshift bins. Note that this broadening is unlikely to be due to larger errors in the photometry of higher redshift galaxies. The median errors in the $\Delta U-B$ of the AGNs are shown above the histograms and are generally much smaller than the widths of the color offset distributions.

We compare the distributions of the control sample and AGNs using a Kolmogorov–Smirnov (K-S) test, which gives us the probability $P_{\mathrm{K\text{-}S}}$ that the two distributions are drawn from a common parent distribution. $P_{\mathrm{K\text{-}S}}$ for AGNs compared to the general control sample are all less than 1% in all three redshift bins.

7.4. Stellar Mass Selection Effects

We are in a position now to tease apart stellar mass selection effects from factors related to SMBH accretion among X-ray selected AGNs. The right set of panels in Figure 8 compares $\Delta U-B$ distributions of the AGNs (filled histograms) and the mass-matched control sample (open histograms) in the three redshift bins. A simple comparison of the middle and right panels shows that the mass-matched control sample is a much better match to the color distribution of the AGNs than the general control sample. In particular, the range in $\Delta U-B$ and the peak value of the mass-matched histograms are now quite similar to the AGNs. $P_{\mathrm{K\text{-}S}}$ for the mass-matched control sample vary from 36% in the low bin to 85% in the intermediate bin, much higher than for the general control sample.

Simply matching in stellar mass leads to a distribution of $U-B$ colors among inactive galaxies that is much more similar to that of the AGN hosts. This is because X-ray detected AGNs are much more likely to be found in massive galaxies than low-mass galaxies (e.g., Silverman et al. 2009). These massive hosts tend to be redder and have lower levels of star formation than the general population of field galaxies. Simply choosing a control sample to have the same range of mass as the AGNs, as was done for the general control sample, is not sufficient to account

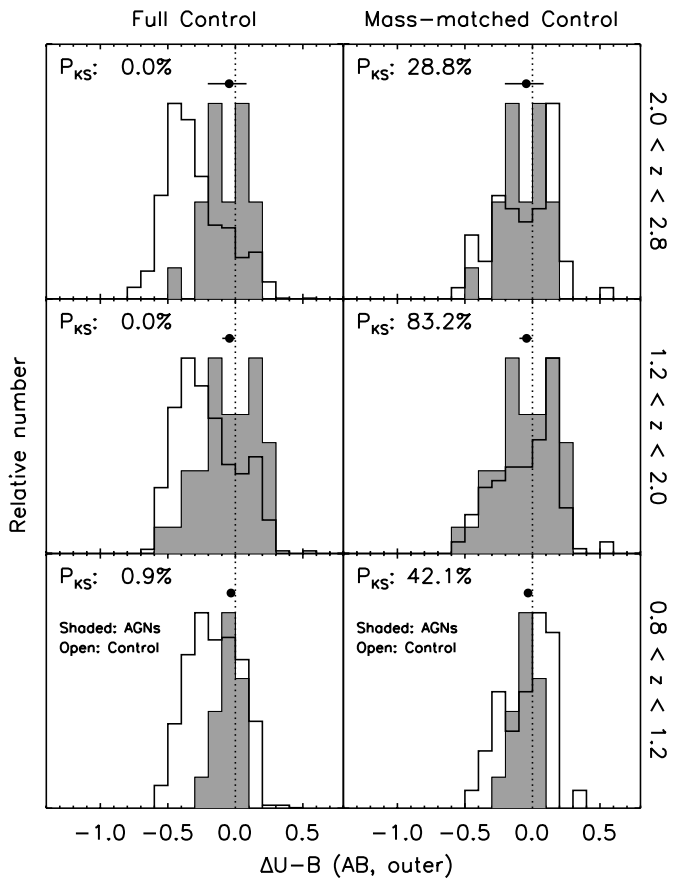

Figure 8. Distributions of outer $U-B$ color offsets from the Green Valley measured in annular apertures of 0.″4–1.″0 in three redshift bins, increasing in median redshift from bottom to top. The left panels show the $U-B$ distribution with respect to the general control sample, while the right panels are a comparison to the mass-matched control sample. The Kolmogorov–Smirnov probability $P_{\rm K\text{-}S}$ is a measure of the likelihood that the two distributions are derived from the same parent distribution. The dashed line marks $\Delta U-B=0$, i.e., the location of the Green Valley. Error bars above the histograms give the median error in the $\Delta U-B$ of the AGNs.

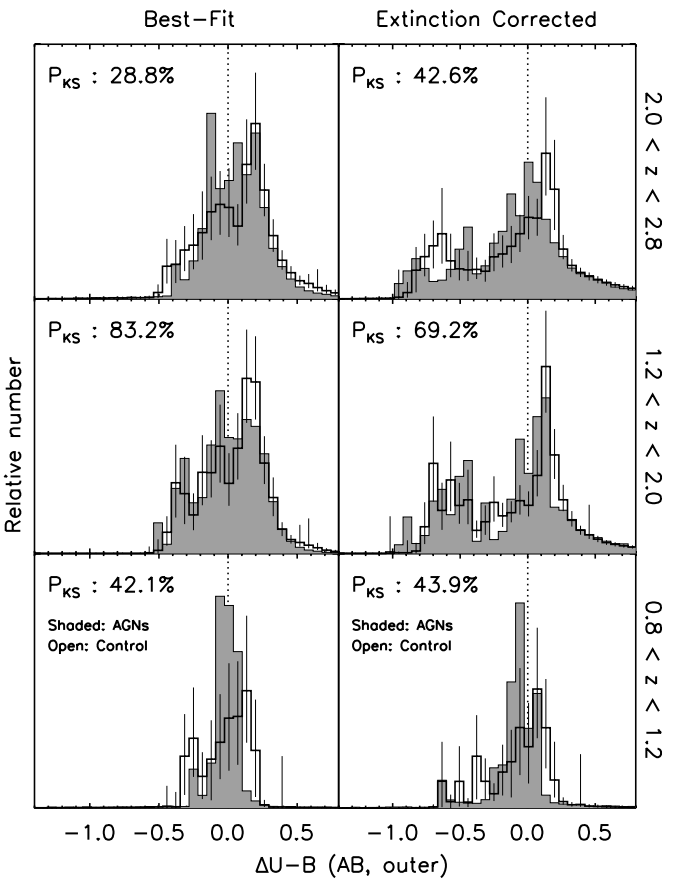

Figure 9. Distributions of outer $U-B$ color offsets from the Green Valley measured in annular apertures of 0.″4–1.″0 in three redshift bins, increasing in median redshift from bottom to top. AGNs are represented by a shaded histogram, while the mass-matched control sample is represented by an open histogram. Error bars on the distributions are combinations of model uncertainties and small sample statistics of the AGNs. The three panels on the left show the distributions of best-fit color, while the panels on the right show the distributions of color for best-fit SED models before applying any extinction (in essence, an extinction-corrected color of the galaxy). These distributions have been regularized by a Monte Carlo bootstrap procedure (Section 5.2). The dashed line marks $\Delta U-B=0$, i.e., the location of the Green Valley.

for stellar mass selection effects. Careful matching of the stellar mass distribution is essential.

We may conclude from this exercise that stellar mass selection effects are the primary cause of any differences in the color distributions of active and inactive galaxies. This is consistent with the results from the study of Xue et al. (2010) using the CDF-S 2 Ms survey.

7.5. AGN Hosts versus Galaxies of Similar M_*

We now turn to a closer examination of the $U-B$ colors of AGN hosts and mass-matched inactive galaxies. The histograms in the right panels of Figure 8 show significant similarities, but some systematic differences remain. However, stochastic effects from the small size of the AGN sample and the large uncertainties in the colors of some galaxies can complicate our interpretation of these differences. In order to account for these effects, we "regularize" the $\Delta U-B$ distributions of the AGNs and mass-matched control sample using the Monte Carlo bootstrapping procedure (Section 5.2). The results are shown in Figure 9. The left panels of the figure plot the regularized distributions of $\Delta U-B$ for AGNs (solid histograms) and mass-matched inactive galaxies (open histograms) in the same three redshift bins. Error bars on the open histograms give the 1σ uncertainty on the distribution of the control sample. As discussed in Section 5.2, these errors take into account the stochasticity of the small AGN sample size, as well as modeling errors.

We concentrate first on a comparison of AGN host color distributions across redshift. In the low bin, one finds a fairly tight range in $\Delta U-B$, spanning about 0.6 mag and peaking sharply at the Green Valley ($\Delta U-B=0$). In the intermediate and high bins, the peak offset still remains roughly fixed. However, the width of the distribution changes considerably between the higher redshift bins and the low bin, with a larger scatter toward red and blue colors. The largest increase is in the fraction of galaxies with blue $U-B$ colors (negative $\Delta U-B$). Since we have removed cases where blue nuclear light could potentially contaminate extended light in the AGN hosts, this evolution in color is likely a consequence of younger light-weighted mean ages in high-redshift AGNs compared to low-redshift AGNs, as well as evolution in the mean metallicity and dust obscuration with redshift. A very similar evolution in the $U-B$ color distribution is also evident in the mass-matched control sample. This underlines the fact that this color evolution is not due to any increasing contribution from AGN light, as this would not be manifested among inactive galaxies.

Comparing now the color distributions of AGN hosts and control galaxies in the left panels of Figure 9, we see that, by and large, the histograms are quite similar in all the redshift bins, as was the case for the unregularized distributions. There may remain a marginal tendency for the modal colors of the AGNs to be bluer than the control sample, but the differences in the overall distributions are minor and not significant, consistent with the high $P_{\rm K\text{-}S}$ values from the K-S tests.

While the general consistency between the colors of AGNs and inactive galaxies of the same stellar mass implies that their stellar populations are also quite similar, certainly when compared to the general field population, one may wonder if other effects could influence this interpretation. For example, could differences in the level of dust obscuration in AGN hosts hide possible differences in stellar populations? For example, Cardamone et al. (2010) find that the application of a dust obscuration correction to the colors of AGN hosts at $z \approx 1$ leads to a pronounced bimodality, paralleling the properties of normal Green Valley galaxies. To explore possible effects from dust obscuration, we plot, in the right panels of Figure 9, distributions of the intrinsic $\Delta U - B$ for the AGN hosts and mass-matched control galaxies. The intrinsic $U - B$ colors come from the population synthesis fits after disregarding the fitted extinction.

Comparing intrinsic and measured color distributions (right and left panels, respectively), one sees that dust obscuration acts to move some galaxies with very blue intrinsic colors (young mean ages) toward the red, tightening the overall color distribution of galaxies. In the right panels, the color distributions of both AGNs and inactive galaxies are now much broader, with a much more pronounced and bluer cloud of star-forming galaxies, especially among the inactive sample. However, the trends that appear in the left panels are also repeated in the right panels. The significant tendency for AGN colors in the low bin to peak in the Green Valley remains, at odds with the results of Cardamone et al. (2010). In the intermediate and high bins, the AGNs and control galaxies show rather similar distributions, with a small, barely significant tendency to peak at colors that are ∼0.1 mag bluer than the peak of the mass-matched control galaxies, placing them marginally closer to the Green Valley.

Before embarking on an interpretation of these color differences, we explore the degree to which such differences arise simply from the limitations of the mass-matching process. The CMD_* in the top panels of Figure 7 indicates that the fraction of blue galaxies increases greatly among the field galaxy population toward higher redshifts. Since we have allowed the mass-matched control sample to include galaxies that can be as much as a factor of two less massive than the AGN hosts, a larger fraction of lower-mass blue galaxies will make it into the control set toward progressively higher redshifts, due to greater errors in the stellar masses and the much greater density of blue galaxies. For these reasons, a general trend toward increasing numbers of blue galaxies among the inactive sample compared to AGNs may be expected from the finite tolerances of the mass-matching procedure.

7.6. Effect of Redshift Errors

The $U - B$ color is sensitive to the strength of the 4000 Å break and hence to the light-weighted mean age of the stellar population of a galaxy. However, in real galaxy catalogs with redshift errors, the error in the color can depend in a complex manner on the redshift errors of the galaxy. If the redshift of a galaxy is in error, the synthetic photometry from SED fits will span wavelengths blueward or redward of the break, where the slope of the galaxy spectrum tends to be shallower than across the actual break. Hence, redshift errors tend to lead to bluer $U - B$ colors irrespective of the sign of the error.

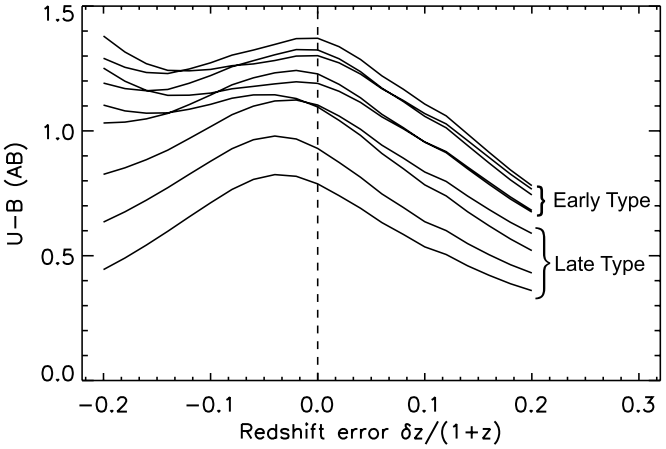

Figure 10. Effects of redshift errors on the $U - B$ colors of galaxies. Each line tracks the color of a certain spectral template of a model galaxy as the redshift error δz is increased or decreased by up to 20% of $1 + z$. Due to the sharpness of the Balmer/4000 Å break, redshift errors tend to lead to bluer colors, irrespective of the sign of the error. The characteristic redshift error of galaxies in this study is $|\delta z/(1 + z)| = 0.07$.

This is potentially important since a large number of our high-redshift AGNs and more than 50% of the control galaxy sample do not have highly accurate spectroscopic redshifts, but instead have photometric redshifts with considerable uncertainty. The characteristic absolute value of $\delta z/(1 + z)$ for galaxies with photometric redshifts in the mass-matched control sample is 0.07, and around 90% have an estimated $|\delta z/(1 + z)| < 0.1$. Hence, one may expect that model $U - B$ colors for the objects with photometric redshifts would be preferentially bluer, which may affect the comparative color studies of previous sections.

The degree of this effect is shown in Figure 10, in which we have plotted simulated $U - B$ colors for a set of representative galaxy spectral templates from the SWIRE template library (Polletta et al. 2007); three quiescent galaxy templates with ages between 2 and 13 Gyr ("Ellipticals") and six star-forming galaxies with varying degrees of current star formation ("Spirals"). The galaxy templates were shifted in wavelength to simulate the effects of a redshift error δz, parameterized in the figure by the $\delta z/(1+z)$. The simulated colors are reddest at δz between -0.02 and 0.0, depending on the template, but get progressively bluer as the redshift errors get both larger and smaller. Due to the sharpness of the 4000 Å break, redshift errors tend to lead to bluer colors, irrespective of the sign of the error.

We constrain the importance of this effect on our rest-frame colors by comparing the $U - B$ distributions of the mass-matched control galaxies with and without spectroscopic redshifts. In Figure 11, we plot the $U - B$ colors of these two sets of control galaxies against redshift. The distribution of the black points (galaxies with photometric redshifts) is very similar to that of the red points (galaxies with spectroscopic redshifts) and clearly does not appear to be systematically bluer. At the highest redshifts ($z \sim 2.5$), the objects with spectroscopic redshifts tend to be a little bluer, probably because bright FUV continua and strong line emission, both associated with blue star-forming galaxies, are a necessary prerequisite for these spectroscopic redshifts.

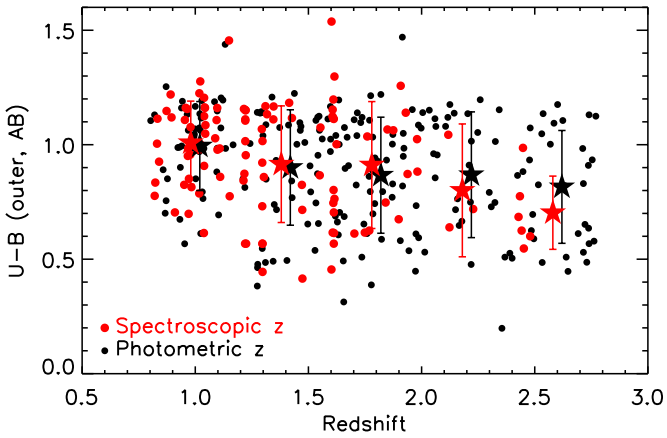

Figure 11. Rest-frame outer $U-B$ color vs. redshift of inactive galaxies from the mass-matched control sample. The black points are galaxies with purely photometric redshifts, while the red points are galaxies with spectroscopic redshifts. The red and black points have very similar color distributions, which implies that the effect of photometric redshift errors on the color distributions of the control sample (see Figure 9) is small to negligible. The mean colors in five redshift bins are shown as large star-shaped points. Beyond a redshift of 2, the objects with spectroscopic redshifts tend to have slightly bluer colors than objects with photometric redshifts, presumably because of selection effects that favor blue star-forming galaxies with emission lines or strong Lyman breaks in such high-redshift spectroscopic samples.

(A color version of this figure is available in the online journal.)

From this we can conclude that photometric redshift errors for the control sample do not introduce strong systematics in the $U-B$ color distributions of the galaxies. A likely cause for the weakening of this effect is that galaxies with prominent spectral features, such as breaks, usually have better-determined photometric redshifts as a consequence of the sharpness of the break, which works against the severity of the effect. The trends in Figure 9 are likely to reflect the true colors of the AGN and control galaxies.

8. COLOR GRADIENTS

Radial color gradients are an important constraint on the role of nuclear activity in the regulation of star formation in AGN hosts. If AGNs are directly responsible for the shutdown of star formation in massive galaxies, a difference is expected in the gradients of AGNs and inactive galaxies of a similar stellar mass. The timescale over which feedback from an AGN blows out a galaxy's gas will determine the steepness of the gradient. The luminosity of the AGN is likely to regulate the scale over which the gradient may be measured—low-luminosity AGNs only supply enough energy and radiation pressure feedback to influence the very inner parts of a galaxy.

In Figure 12, we compare the gradients in the rest-frame $U-B$ colors of the AGNs (large colored star points) and mass-matched control sample (small black points) against their outer $U-B$ colors, in two redshift bins. Gradients are calculated as the difference between the outer and nuclear $U-B$ colors, i.e., colors from fixed apertures of radius 0.″4–1.″0 (annular) and 0.″1, respectively. A lower/higher value of the gradient implies a bluer/redder outer color, with the dotted line showing a flat gradient. In addition, we use colors for the star points to indicate the X-ray luminosity of the AGNs, from $L_{2-10} = 10^{42}$ (black stars) to $L_{2-10} = 10^{44.5}$ (red stars). The AGNs with nuclear contamination are included in the figure as large concentric star points.

A first observation is that the median gradient of both uncontaminated AGNs and control galaxies is negative, with most points lying below the flat-gradient dotted line. Therefore, both AGNs and inactive galaxies are generally redder in the central few kpc, compared to their outskirts. The median offset from a flat gradient varies from ≈ -0.16 in Bin A to ≈ -0.25 in Bin C. The scatter in the gradient also increases considerably toward high redshifts. The source of this change in the median and the scatter could be intrinsic to the galaxy population, but it is also influenced by the accuracy of PSF matching (to which the nuclear colors are particularly sensitive), as well as the larger errors in photometry suffered by the more distant galaxies. This is why a careful control sample processed through the same selection criterion, photometric measurement, and modeling method is critical to constrain true differences in the color gradients between AGNs and normal galaxies.

In general, the form and scatter of the distribution of color gradients between uncontaminated AGNs and inactive galaxies

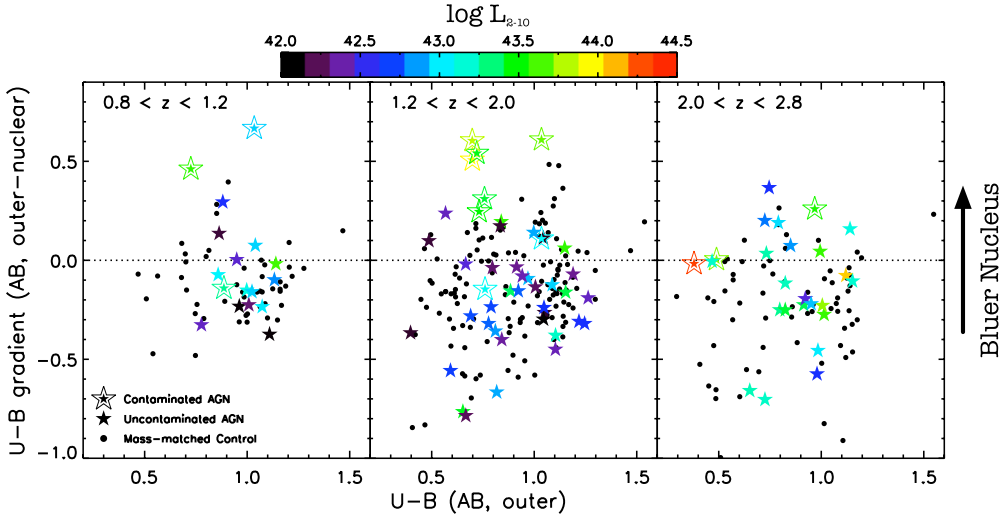

Figure 12. Rest-frame $U-B$ color gradients (outer-nuclear) plotted against the outer $U-B$ color, in three redshift bins. AGNs are shown by colored star points, where the color represents the hard-band X-ray luminosity L_{2-10} (as shown by the color bar). Sources with nuclear contamination are marked with concentric star points. The small black points are the mass-matched control sample of inactive galaxies.

(A color version of this figure is available in the online journal.)

are similar, implying that the presence of the AGN does not strongly influence the distribution of SF in their hosts. This, coupled with observation that the outer colors of AGN hosts are consistent with those of normal galaxies of the same mass, suggests that the outer stellar populations of AGN hosts are the suppression of star formation by feedback effects. This does not extend beyond a few kpc, at least for AGNs in the luminosity range probed by our sample ($L_{2-10} \lesssim 45$ erg s^{-1}).

9. STAR FORMATION HISTORIES OF AGN HOSTS

The detailed sampling of the SEDs of AGNs and control galaxies over six to seven broad photometric bands enables a determination of the light-weighted SFHs parameterized by a suite of increasing and decreasing τ models and constant star formation rate models (Section 5).

Before proceeding with an examination of SFH parameters, we highlight the dominance of exponentially decreasing SFHs among AGNs and similar-mass galaxies. This is consistent with their high stellar masses and relatively red colors, even out to $z \sim 3$. Among AGNs and control galaxies in the low bin ($0.8 < z < 1.2$), essentially none have flat or rising SFHs for the best-fit models. The fraction of galaxies with non-declining SFHs increases in the intermediate and high bins (13% at $1.2 < z < 2.0$ and 23% at $2.0 < z < 2.8$) but is still quite low. The rates of best-fit rising SFH models are as common among X-ray AGNs as among inactive galaxies.

The light-weighted stellar age is one of the fundamental physical characteristics of the SFH of galaxies. However, typically the age is quite hard to estimate accurately as it can be degenerate with both the metallicity of the stellar population and the level of dust extinction. Therefore, the confidence intervals on the stellar age from our SED fits can be quite large and are typically skewed toward young ages. In order to make statistically valuable conclusions about the age distributions of the AGNs and their comparisons with normal galaxies, we apply our bootstrap regularization procedure to arrive at more representative age distributions for the galaxies.

The results are shown in the left panels of Figure 13. As before, the AGNs are shown as a shaded histogram, while the control sample is shown as an open histogram, in the low-, intermediate-, and high-redshift bins. The $P_{\rm K\text{-}S}$ values in these panels come directly from K-S tests on the original distributions, not the regularized distributions shown in the panels. They are a measure of the consistency of the age distributions without taking into account the skewed uncertainties on best-fit ages. In the low bin, the control galaxies show a relatively broad range of ages. The AGNs have a distribution that is a bit narrower than the control sample, but not significantly. To the uncertainties of the sample, the distributions are very similar.

In the higher-redshift bins, the sample sizes of AGNs (and, by extension, mass-matched control galaxies) are 2–3 times larger, making for better-defined age histograms. The control galaxies in the intermediate and high bins show a broad but definite peak at 2 Gyr and another smaller narrow peak at ≈100 Myr. Compared to the low bin, there is a larger fraction of inactive galaxies with younger ages, stretching down to our lower age limit of 10 Myr. This is consistent with the larger fraction of blue galaxies at higher redshifts among the mass-matched sample and the AGN hosts.

The AGNs in the intermediate and high bins again appear to be quite similar to the control sample, though in both bins, the AGN distribution is a bit narrower than the control. In addition, in both bins, the AGNs do not show the second peak in the age

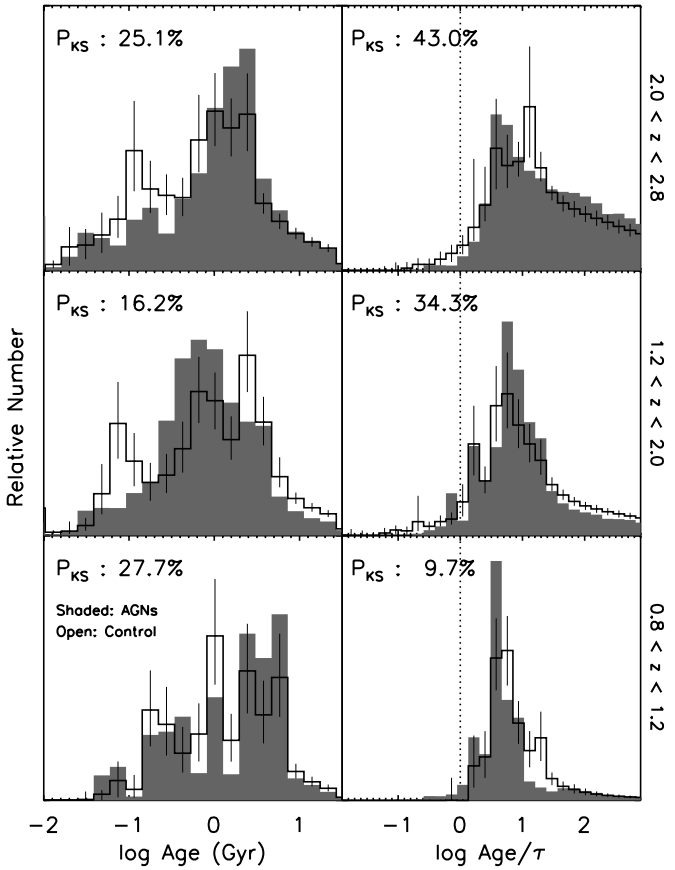

Figure 13. Comparison of the distributions of the light-weighted ages (left panels) and "normalized ages" (right panels) of AGNs and control galaxies estimated from photometry in extended-light apertures. AGN hosts (gray histograms) are compared to mass-matched inactive galaxies (open histograms) in three redshift bins, as indicated. Distributions have been regularized by a Monte Carlo bootstrap procedure (Section 5.2). Error bars on the control galaxy histograms show the approximately 1σ variation in the distributions for sample sizes comparable to those of the AGN hosts. In each panel, the two-sided Kolmogorov–Smirnov probability $P_{\rm K\text{-}S}$, measured on the unregularized data, compares the similarity of the two distributions.

distribution at young ages that is seen in the control sample. This difference is fairly significant (≈2σ at ages $\lesssim 0.1$ Gyr) but may be related to the limitations of mass matching at higher redshifts.

We also explore, from our SFHs, the degree to which AGN hosts have built up their stellar content at all these redshifts. We define a parameter called the "normalized age," which is the ratio of stellar age to τ. This parameter, for declining τ models, indicates how much older a particular galaxy is compared to the timescale over which most of its stars form. In the right panels of Figure 13, we compare normalized age histograms of AGNs and control galaxies in our three redshift bins, derived from our SED fits and regularized using the bootstrap procedure. Only objects with declining τ models are used in these histograms, since the normalized age has a different interpretation for exponentially increasing or constant SFH models.

One may see that at all redshifts considered, the normalized age distributions for AGNs and control galaxies peak at values greater than 1. The distribution is quite narrow at $z \sim 1$ but gets progressively broader at higher redshifts as a strong tail develops to high values. This is because τ is weakly constrained among faint high-redshift galaxies and low τ values lead to progressively higher normalized ages.

In the intermediate and high bins, the peaks and widths of the AGN and control distributions are very similar. In the low-redshift bin, however, a K-S test suggests that the best-fit normalized ages of AGNs and control galaxies differ significantly, with a $P_{\text{K-S}} \lesssim 10\%$ that they are drawn from the same parent distribution. The regularized histograms at normalized ages $\gtrsim$10 differ at the level of a few σ, showing that the AGNs display a narrow distribution of normalized ages and a weaker tail to long ages than the control sample. In essence, this means that at $z \approx 1$, the normalized ages of AGNs are slightly shorter and have less variation than inactive galaxies of the same mass.

10. DISCUSSION

10.1. The Colors and SFHs of AGN Hosts

With the high spatial resolution and unparalleled sensitivity of the WFC3 camera, we have examined the photometric properties and SFHs of AGN host galaxies in the CANDELS/CDF-S field at redshifts of $0.8 < z < 2.8$, while avoiding complications arising from strong nuclear contamination. Consistent with earlier studies, X-ray selected AGNs are found to reside in galaxies that are significantly more massive than the general field galaxy population (e.g., Silverman et al. 2009). The typical stellar mass of AGN hosts is $\log M_* \sim 10.5$, and it changes very little (less than a factor of 3) toward high redshifts. This suggests that low- to intermediate-luminosity AGNs reside in hosts of a characteristic stellar mass over a large range in redshift.

In keeping with their high stellar masses, AGN hosts are more likely to be found in galaxies with red or intermediate colors, compared to the general population of field galaxies. To account for covariances in galaxy properties that are a strong function of stellar mass, we make a detailed comparison of the colors, color gradients, and SFHs of AGN hosts to a comparison sample of inactive galaxies that are matched in stellar mass to the AGNs.

We find that, to a major degree, AGN hosts at all redshifts have basic photometric properties—rest-frame colors, extinctions, and color gradients—that are similar to mass-matched inactive galaxies. AGN hosts get considerably bluer and more compact toward higher redshifts, but this evolution is consistent with the changes seen in the inactive galaxy population as well. In addition, both AGNs and inactive galaxies show typically old stellar populations (ages $\gtrsim$ 1 Gyr) and are better fit by models with a declining SFH at all redshifts (though the fraction of galaxies with flat or rising SFHs increases with redshift). The characteristic age of AGNs is long compared to the timescale of SF (i.e., τ for exponentially declining SF models). In essence, low- to moderate-luminosity AGNs are found in relatively normal massive galaxies at all redshifts to $z = 3$.

10.2. AGNs and the Transformation of Galaxies

Several studies have suggested that the high frequency of AGNs in the Green Valley is evidence of a close association between the quenching of star formation in galaxies and the feedback from active nuclei (Nandra et al. 2007; Schawinski et al. 2007, 2010). According to this scenario, the energy output of the accreting SMBH couples with the gas in the disk of a star-forming blue cloud galaxy and either drives most of it out of the galactic potential (Kaviraj et al. 2011) or, alternatively, heats it to a temperature beyond 10^6 K. At this point, the gas is too hot or too diffuse to cool back into the galaxy disk and the star formation shuts down. The timescale of AGN-driven quenching is short enough (0.5 Gyr) that the galaxy's light is dominated by an intermediate-age stellar population with colors typical of the Green Valley. The relative infrequency of Green Valley galaxies, reflected in the color bimodality of the galaxy population, is a consequence of the rapidity of AGN-driven quenching. A similarity between the estimated timescales of AGN activity and the timescales needed to move a quenched galaxy onto the Red Sequence seems to imply a close association between the two processes (Schawinski et al. 2007; Bundy et al. 2008). Schawinski et al. (2007) also find close associations between a population of local blue early-type galaxies and AGN activity, indicating that AGNs may play a role in the quenching of ongoing star formation in such systems.

However, an elevated fraction of AGNs in the Green Valley can also arise from a simple phenomenological explanation, which does not require a strong role for AGN feedback in the transformation of galaxies (Sánchez et al. 2004; Silverman et al. 2009). Two key ingredients necessary for producing an AGN are (1) fuel, in the form of relatively cold interstellar gas in the host galaxy, and (2) a super massive black hole. For an accreting black hole of a given mass to be detected at intermediate to high redshifts in a typical deep flux-limited X-ray survey, it needs to have either a high accretion rate (or Eddington ratio), a high black hole mass, or both. Since massive black holes are typically found in galaxies with massive spheroids (e.g., Häring & Rix 2004), the detection rate of X-ray AGNs will increase with bulge fraction and stellar mass, but to a point. The most massive galaxies at essentially all redshifts are almost always elliptical galaxies, which have hot halos and are deficient in cold gas, due to heating in virial shocks (Birnboim et al. 2007), feedback from radio jets (Best et al. 2006; Croton et al. 2006), or strong "quasar mode" feedback during a possible earlier major merger episode (e.g., Urrutia et al. 2008). Such systems are unlikely to host black holes that accrete significant quantities of cold gas. Therefore, in this picture, X-ray AGNs are preferentially found in galaxies with massive spheroids (and black holes), but also with disks that contain sufficient cold gas to keep up regular cycles of accretion. Such galaxies are typical of the Green Valley (Cassata et al. 2007). In this scenario, the prevalence of AGNs in galaxies with intermediate colors is solely a consequence of the necessary conditions for an accreting black hole to be detected in X-rays, coupled with a static or redshift-dependent relationship between SMBHs and spheroids (e.g., Tremaine et al. 2002; Merloni et al. 2010; Bennert et al. 2011; Kormendy et al. 2011), which is probably set during high accretion rate phases, such as through galaxy mergers (Hopkins et al. 2008b). Considerable scatter in the location of AGNs in the color–mass diagram would be naturally expected, mostly toward redder galaxy colors, since some early-type galaxies are known to contain a sizable amount of cold dusty nuclear gas (Ferrarese et al. 2006), possibly through settling of dense gas in hot atmospheres or mass loss from evolved stars.

If AGN hosts are indistinguishable from a population of massive inactive galaxies of the same stellar mass, this would support the latter scenario. In this scenario, the characteristics of AGN hosts would be set not by their nuclear activity, but by the strong dependence of galaxy properties on stellar mass, modulated by the conditions necessary to fuel SMBH accretion (massive bulge and gas-rich disk). On the other hand, if AGN hosts deviate from inactive galaxies of the same stellar mass in a systematic way, this could indicate that nuclear activity does in fact play a role in determining the gross properties of the hosts and lend support for a more intimate two-way connection between AGNs and their hosts.

Unfortunately, our study is somewhat inconclusive in this regard. We can say for certain that a large part of the typical properties of AGN hosts are set by their stellar mass, rather than the fact that they host an accreting SMBH. This is clear since AGNs for the most part are really quite similar to inactive galaxies of the same mass. This rules out any models that postulate strong differences between the AGN and normal galaxy population, for, e.g., models that tie most nuclear activity to galaxy mergers or post-mergers. Such a result is consistent with recent studies that find that AGNs have very similar morphologies to inactive, mass-matched galaxies across redshifts we consider in this work (Cisternas et al. 2011; Schawinski et al. 2011; Kocevski et al. 2012).

We notice some possible minor differences at $z \sim 1$—for, e.g., the tendency for AGN hosts to have a narrow range in $U-B$ color and have shorter normalized ages than inactive galaxies—which should not be strongly affected by systematics in the construction of a control sample. These results are qualitatively consistent with earlier studies of AGN hosts at $z \sim 1$ (e.g., Sánchez et al. 2004; Gabor et al. 2009), though stellar mass selection effects were not fully taken into account in much prior work. In general, AGNs have a tendency toward older stellar ages, but a slightly higher fraction of them have formed stars more recently. These two apparently opposing notions may be reconciled if AGN hosts have older formation times but broader SF timescales than inactive galaxies. In other words, they have formed a small fraction of stars more recently, possibly in association with the process that drives accretion.

At higher redshifts, these differences become less pronounced and more susceptible to systematics. Our intermediate-redshift bin ($1.2 < z < 2.0$) has the best statistics, low incompleteness, and stellar mass uncertainties that are not too severe. In this bin, we find that AGNs are most closely similar to inactive galaxies.

If AGNs are no different from inactive galaxies, or associated with low levels of recent star formation, then the importance of AGNs as mechanisms for driving the prompt transformation of galaxies from star-forming to quiescence may be overstated. Such models predict that AGNs are in galaxies with less recent SF, not more, since the phase of AGN activity leads to the immediate quenching of star formation, while in galaxies without AGNs, star formation can proceed unabated. However, a possible variation on this scenario may be able to reconcile our observations with a role for AGN feedback. If AGN activity is synchronized with star formation phases, it is possible that feedback may effectively shorten the timescale of star formation and therefore reduce the efficiency of star formation in these massive galaxies. In such a scenario, AGN hosts contain signatures of recent star formation because it is only in galaxies with such recent star formation that AGNs have been triggered, possibly by the same process that triggered the formation of stars as well. Such processes could be for, e.g., minor mergers or satellite interactions, bar instabilities, or the infall of fresh gas from the intergalactic medium. The feedback from the active nucleus would then cut short a burst of star formation that would have continued longer had the AGN not been present. In this way, by gradually eroding the duty cycle of star formation in massive galaxies, AGNs may be able to play a role in their transformation.

10.3. Evolution in the Relationship of AGN Hosts to Normal Galaxies?

From a large study of the morphologies and colors of AGN hosts in the Galaxy Zoo survey, Schawinski et al. (2010) find that local AGNs satisfy a strong preference for the Green Valley, even when mass selection effects are taken into account. In particular, the most massive local galaxies are less likely to host AGNs compared to galaxies that have bluer colors and lower masses. A recent study of the properties of a hard X-ray selected BAT sample of AGNs (Koss et al. 2011), which span a luminosity range that is similar to the CDF-S 4 Ms sample, also finds a similar result, while again accounting for stellar mass selection effects. Taken at face value, these studies suggest that local AGNs are still preferentially found in the Green Valley and may be more closely associated with a quenching galaxy population.

This contrasts considerably with what we find at $z > 1.5$, where AGN hosts have a similar spread in color and SFH as inactive galaxies of the same mass and indeed are very common among the most massive systems at these redshifts. At $z \sim 1$, our results suggest a situation that is intermediate between these local studies and the properties of AGN hosts at higher redshift. If true, we may be witnessing a change with redshift of the relevant processes that relate substantial black hole accretion to the properties of the host galaxy. The high gas fractions and turbulent, clumpy gas disks seen among massive galaxies at $z \sim 2$ should allow more frequent and consistent inflow of gas to the central SMBH (Bournaud et al. 2011). Such processes will be able to occasionally fuel even more luminous phases, such as quasars, which require disruptive processes like major mergers to drive them at low redshifts. If so, the relative importance of major mergers as the triggers of major SMBH growth at high redshift will decline, while secular processes, such as turbulent accretion, will be more important. This may explain the change in the association between galaxies and AGN activity toward higher redshift: if secular inflow can fuel most AGNs at $z \sim 2$, all galaxies with such gas disks will be able to accrete significant quantities to be able to shine as an X-ray AGN. In this case, every massive galaxy is a candidate AGN host. At lower redshifts, only massive spiral galaxies, with enough gas in their disks, can fuel secular AGN phases, while a larger fraction of Seyfert activity is fueled in post-merger systems (Schawinski et al. 2010). This will naturally lead to an evolution in the make up of AGN hosts toward higher redshifts.

A deeper understanding of the physics of feedback, from simulations (e.g., Debuhr et al. 2010) and observations of active galaxies across a range of scales, is crucial toward constraining whether, how, where, and when AGNs play a part in altering the nature of their hosts. Our study allows us to rule out the importance of strong and prompt quenching in AGNs, but weaker, longer-lasting, and more pervasive processes could still have a critical role in modulating the transformation of galaxies. In addition, we suggest that evolution in the principal mode of AGN fueling may be relevant in studies of AGN hosts with redshifts. As the CANDELS survey expands, we will be able to study thousands of AGNs across a wide range of redshifts with this remarkable data set and, hopefully, tease apart the various roles of galaxy mass, gas inflow, AGN luminosity, and feedback in the evolution of active galaxies.

We thank S. M. Ammons and F. Bournaud for fruitful discussion. This work is based on observations taken by the CANDELS Multi-Cycle Treasury Program with the NASA/ESA *HST*, which is operated by the Association of Universities for Research in Astronomy, Inc., under NASA contract NAS5-26555. This research has made use of data obtained from the Chandra Data Archive and the Chandra Source Catalog and

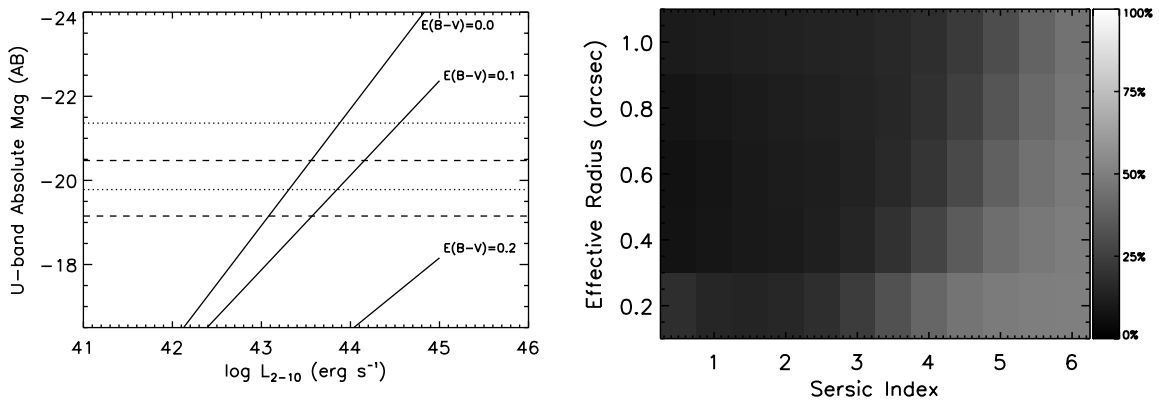

Figure 14. Left panel: the *U*-band absolute magnitude of nuclear emission from an AGN as a function of the X-ray luminosity of the AGN, for three values of nuclear dust extinction $E(B-V)$. These estimates were made assuming the X-ray to mid-IR correlation of local AGNs from Gandhi et al. (2009) and a mean Type I AGN SED to connect the UV to the mid-IR. The typical ranges of *U*-band luminosities of normal massive galaxies in FIREWORKS at $0.8 < z < 1.2$ (dashed lines) and $2.0 < z < 2.8$ (dotted lines) are shown. At modest levels of extinction, even the most luminous AGNs in our sample are too faint to adversely contaminate the photometry of the host. Only if an AGN is quite unobscured can it dominate the galaxy's integrated photometry. Right panel: the fractional increase in the annular flux over the light of a galaxy due to the presence of a bright nuclear point source, for model galaxies with a range in size and Sérsic profile index. The circular annulus spans galaxy radii from 0.″4 to 1″, matching the annulus used for extended-light photometry in this paper. In the case shown here, the point source is assumed to contain as much flux as the galaxy. Such AGNs can be easily identified visually unless the point source is reddened considerably by dust. For the luminosity range of AGNs in our work, dust extinction will also strongly reduce the UV contribution from any point sources. AGN contamination is therefore unlikely to be a large source of systematics in this study.

software provided by the Chandra X-Ray Center (CXC) in the application packages CIAO, ChIPS, and Sherpa.

APPENDIX

EFFECTS OF AGN POINT-SOURCE CONTAMINATION ON APERTURE PHOTOMETRY

The CANDELS WFC3 F160W point-spread function has fairly bright wings relative to its core, particularly when compared to the ACS PSF (95% encircled energy radii of 0.″8/1.″5 for ACS F814W/WFC3 160W). Therefore, one must understand the effects of scattered light on aperture photometry before interpreting such measurements, especially in AGNs, which can display strong nuclear point sources.

We approach this in a two-part manner. We first predict the expected luminosity of AGN point sources in the rest-frame *U* band and compare these predictions to the luminosities of massive galaxies at the redshift range of our sample. From this input, we evaluate the range of point-source-to-galaxy flux ratios that our sample of AGNs is expected to show in the bluest bands. Next, we use a suite of simulated galaxies with added central point sources to evaluate the effects of AGN contamination on extended aperture photometry as a function of galaxy size, Sersíc index, and point-source fraction.

The hard-band X-ray luminosity of local AGNs is known to correlate quite well with their nuclear MIR luminosity over a large range in intrinsic AGN luminosity. Specifically adopting the L_{2-10}-to-12.3 μm relationship from Gandhi et al. (2009), and using model Type 1 AGN SEDs to connect the rest-frame *U*-band luminosity to the MIR, we can predict the relationship between L_{2-10} and M_U for the X-ray luminosity range of our AGN sample. The effects of nuclear dust obscuration can also be explored by applying a range of extinction to the model AGN SEDs. We adopt a moderate-luminosity Type 1 AGN SED from Silva et al. (2004) and Galactic screen extinction (the results are not very sensitive to the choice of extinction law or mean AGN SED template). The left panel of Figure 14 summarizes this exercise. For AGNs with a given hard-band X-ray luminosity, we plot solid lines that show the expected *U*-band luminosity for AGNs as a function of L_{2-10} for three different values of $E(B-V)$. In addition, we show the 1σ range in absolute *U* magnitude for inactive galaxies with stellar masses similar to the AGNs in the redshift ranges $0.8 < z < 1.2$ and $2.0 < z < 2.8$ (dashed and dotted lines, respectively).

From the figure, we deduce that *unobscured* AGNs ($E(B-V)=0$) with $L_{2-10} > 10^{43}$ erg s^{-1} have point-source luminosities that rival the total luminosity of galaxies across all redshifts in this work. However, even small levels of nuclear obscuration quickly depress the rest-frame *U*-band luminosity of the AGN, such that point sources with a modest $E(B-V)=0.2$ are more than a magnitude fainter than most galaxies, even among the most luminous AGNs in our sample ($L_{2-10} \sim 10^{45}$ erg s^{-1}). Since the intrinsic emission from an AGN rises sharply through blue and UV wavelengths, we expect the nuclear colors of AGNs with strong nuclear point-source contamination to be overwhelmingly blue. Obscured AGNs may display red point sources, but they are not expected to be very luminous in comparison to the host galaxy for the nuclear luminosities and redshifts considered by this study.

This is supported by observations. X-ray selected AGNs at $z < 1.5$ in the CDF fields appear to show pervasive central point sources, attributed by some authors to highly reddened nuclear emission (Ballo et al. 2007; Simmons et al. 2011). The typical extinctions of these point sources were $E(B-V) > 0.1$, and they accounted for lower than 10% of the total luminosity of the host. Gabor et al. (2009) performed a similar exercise on AGNs from the COSMOS field, which tend to more luminous than the sample considered in this work. Even so, only a handful of AGN point sources from their study were as luminous as their host galaxies.

For the second part of our analysis of AGN contamination, we simulated a suite of model circular galaxies with Sersíc light profiles (index $n = 0.5$–6) and half-light radii in the range $R_{\rm eff} = 0.″2$–$1.″5$. After convolving the galaxies by the WFC3 F160W PSF (described in Section 2.1), we added a point source to the images, scaled to a total point-source-to-galaxy flux ratio in the range $R_{\rm PS} = 0.01$–2.0. In the right panel of Figure 14, we plot the fractional increase in flux in the extended-light

aperture (0.″4–1.″0, used for all photometry in this paper) due to a central point source of $R_{PS} = 1$. Sources with such bright point sources would be easily identified visually as bright blue compact structures in the centers of these galaxies.

For galaxies with typical sizes ($R_{eff} > 0.''4$) and Sersíc indices (1–4) found among AGN hosts, a bright point source adds around a few tens to fifty percent more light in this aperture over the light from the galaxy. Among AGNs with such strong nuclear emission, our extended-light photometry is contaminated by the central source less than the integrated photometry of the galaxy. Since point sources are generally more compact than galaxies, extended light among fainter AGNs is proportionately contaminated even less than in bright AGNs. Through the application of our X-ray parameter-based cuts to exclude luminous, unobscured AGNs, we remove all cases of strong nuclear point sources. Among the remaining AGNs, nuclear contamination in the outer apertures is quite minimal and will not strongly influence our results.

REFERENCES

Antonucci, R. 1993, ARA&A, 31, 473
Arnouts, S., Walcher, C. J., Le Fèvre, O., et al. 2007, A&A, 476, 137
Baggett, S. M., Hill, R. J., Kimble, R. A., et al. 2008, Proc. SPIE, 7021, 70211Q
Ballo, L., Cristiani, S., Fasano, G., et al. 2007, ApJ, 667, 97
Bauer, F. E., Alexander, D. M., Brandt, W. N., et al. 2002, AJ, 124, 2351
Bennert, N., Canalizo, G., Jungwiert, B., et al. 2008, ApJ, 677, 846
Bennert, V. N., Auger, M. W., Treu, T., Woo, J.-H., & Malkan, M. A. 2011, ApJ, 742, 107
Benson, A. J., Bower, R. G., Frenk, C. S., et al. 2003, ApJ, 599, 38
Best, P. N., Kaiser, C. R., Heckman, T. M., & Kauffmann, G. 2006, MNRAS, 368, L67
Birnboim, Y., Dekel, A., & Neistein, E. 2007, MNRAS, 380, 339
Bournaud, F., Dekel, A., Teyssier, R., et al. 2011, ApJL, 741, 33
Bower, R. G., Benson, A. J., Malbon, R., et al. 2006, MNRAS, 370, 645
Boyle, B. J., & Terlevich, R. J. 1998, MNRAS, 293, L49
Brammer, G. B., van Dokkum, P. G., & Coppi, P. 2008, ApJ, 686, 1503
Brusa, M., Fiore, F., Santini, P., et al. 2009, A&A, 507, 1277
Bruzual, G., & Charlot, S. 2003, MNRAS, 344, 1000
Bundy, K., Georgakakis, A., Nandra, K., et al. 2008, ApJ, 681, 931
Calzetti, D., Kinney, A. L., & Storchi-Bergmann, T. 1994, ApJ, 429, 582
Cardamone, C. N., Urry, C. M., Schawinski, K., et al. 2010, ApJL, 721, 38
Cassata, P., Guzzo, L., Franceschini, A., et al. 2007, ApJS, 172, 270
Cattaneo, A., Faber, S. M., Binney, J., et al. 2009, Natur, 460, 213
Cisternas, M., Jahnke, K., Inskip, K. J., et al. 2011, ApJ, 726, 57
Conroy, C., Gunn, J. E., & White, M. 2009, ApJ, 699, 486
Croton, D. J., Springel, V., White, S. D. M., et al. 2006, MNRAS, 365, 11
Debuhr, J., Quataert, E., Ma, C.-P., & Hopkins, P. 2010, MNRAS, 406, L55
Dunlop, J. S., McLure, R. J., Kukula, M. J., et al. 2003, MNRAS, 340, 1095
Ferrarese, L., Côté, P., Dalla Bontà, E., et al. 2006, ApJL, 644, 21
Ferrarese, L., & Merritt, D. 2000, ApJL, 539, 9
Gabor, J. M., Impey, C. D., Jahnke, K., et al. 2009, ApJ, 691, 705
Gandhi, P., Horst, H., Smette, A., et al. 2009, A&A, 502, 457
Gebhardt, K., Bender, R., Bower, G., et al. 2000, ApJL, 539, 13
Georgakakis, A., Coil, A. L., Laird, E. S., et al. 2009, MNRAS, 397, 623
Giavalisco, M., Ferguson, H. C., Koekemoer, A. M., et al. 2004, ApJL, 600, 93
Grogin, N. A., Kocevski, D. D., Faber, S. M., et al. 2011, ApJS, 197, 35
Guo, Y., Giavalisco, M., Cassata, P., et al. 2011, ApJ, 735, 18
Guyon, O., Sanders, D. B., & Stockton, A. 2006, ApJS, 166, 89
Häring, N., & Rix, H.-W. 2004, ApJL, 604, 89
Hook, R., Stoehr, F., & Krist, J. 2008, STECF, 44, 11
Hopkins, P. F., Cox, T. J., Kereš, D., & Hernquist, L. 2008a, ApJS, 175, 390
Hopkins, P. F., Hernquist, L., Cox, T. J., & Kereš, D. 2008b, ApJS, 175, 356
Hopkins, P. F., Richards, G. T., & Hernquist, L. 2007, ApJ, 654, 731
Hunt, L. K., & Malkan, M. A. 1999, ApJ, 516, 660
Jahnke, K., & Macciò, A. V. 2011, ApJ, 734, 92
Kannappan, S. J., & Gawiser, E. 2007, ApJL, 657, 5
Kauffmann, G., Heckman, T. M., Tremonti, C., et al. 2003, MNRAS, 346, 1055
Kaviraj, S., Schawinski, K., Silk, J., & Shabala, S. S. 2011, MNRAS, 415, 3798
Kennicutt, R. C., & Evans, N. J. 2012, ARA&A, 50, 531
Kocevski, D. D., Faber, S. M., Mozena, M., et al. 2012, ApJ, 744, 148
Koekemoer, A. M., Faber, S. M., Ferguson, H. C., et al. 2011, ApJS, 197, 36
Kormendy, J., Bender, R., & Cornell, M. E. 2011, Natur, 469, 374
Koss, M., Mushotzky, R., Veilleux, S., et al. 2011, ApJ, 739, 57
Kriek, M., Labbé, I., Conroy, C., et al. 2010, ApJL, 722, 64
Laird, E. S., Nandra, K., Georgakakis, A., et al. 2009, ApJS, 180, 102
Luo, B., Brandt, W. N., Xue, Y. Q., et al. 2010, ApJS, 187, 560
Magorrian, J., Tremaine, S., Richstone, D., et al. 1998, AJ, 115, 2285
Maraston, C. 2005, MNRAS, 362, 799
Maraston, C., Daddi, E., Renzini, A., et al. 2006, ApJ, 652, 85
Maraston, C., Pforr, J., Renzini, A., et al. 2010, MNRAS, 407, 830
Marchesini, D., van Dokkum, P. G., Förster Schreiber, N. M., et al. 2009, ApJ, 701, 1765
McNamara, B. R., & Nulsen, P. E. J. 2007, ARA&A, 45, 117
Merloni, A., Bongiorno, A., Bolzonella, M., et al. 2010, ApJ, 708, 137
Morganti, R., Tadhunter, C. N., & Oosterloo, T. A. 2005, A&A, 444, L9
Morrison, R., & McCammon, D. 1983, ApJ, 270, 119
Muzzin, A., Marchesini, D., van Dokkum, P. G., et al. 2009, ApJ, 701, 1839
Nandra, K., Georgakakis, A., Willmer, C. N. A., et al. 2007, ApJL, 660, 11
Nandra, K., & Pounds, K. A. 1994, MNRAS, 268, 405
Noeske, K. G., Weiner, B. J., Faber, S. M., et al. 2007, ApJL, 660, 43
Peng, C. Y., Ho, L. C., Impey, C. D., & Rix, H.-W. 2010, AJ, 139, 2097
Pforr, J., Maraston, C., & Tonini, C. 2012, MNRAS, 422, 3285
Pierce, C. M., Lotz, J. M., Laird, E. S., et al. 2007, ApJL, 660, 19
Pierce, C. M., Lotz, J. M., Primack, J. R., et al. 2010a, MNRAS, 405, 718
Pierce, C. M., Lotz, J. M., Salim, S., et al. 2010b, MNRAS, 408, 139
Polletta, M., Tajer, M., Maraschi, L., et al. 2007, ApJ, 663, 81
Pounds, K. A., Reeves, J. N., King, A. R., et al. 2003, MNRAS, 345, 705
Rosario, D. J., Shields, G. A., Taylor, G. B., Salviander, S., & Smith, K. L. 2010, ApJ, 716, 131
Rupke, D. S. N., & Veilleux, S. 2011, ApJL, 729, 27
Salim, S., Charlot, S., Rich, R. M., et al. 2005, ApJL, 619, 39
Salvato, M., Hasinger, G., Ilbert, O., et al. 2009, ApJ, 690, 1250
Sánchez, S. F., Jahnke, K., Wisotzki, L., et al. 2004, ApJ, 614, 586
Schawinski, K., Thomas, D., Sarzi, M., et al. 2007, MNRAS, 382, 1415
Schawinski, K., Treister, E., Urry, C. M., et al. 2011, ApJL, 727, 31
Schawinski, K., Urry, C. M., Virani, S., et al. 2010, ApJ, 711, 284
Schawinski, K., Virani, S., Simmons, B., et al. 2009, ApJL, 692, 19
Silva, L., Maiolino, R., & Granato, G. L. 2004, MNRAS, 355, 973
Silverman, J. D., Lamareille, F., Maier, C., et al. 2009, ApJ, 696, 396
Silverman, J. D., Mainieri, V., Lehmer, B. D., et al. 2008, ApJ, 675, 1025
Silverman, J. D., Mainieri, V., Salvato, M., et al. 2010, ApJS, 191, 124
Simmons, B. D., Van Duyne, J., Urry, C. M., et al. 2011, ApJ, 734, 121
Somerville, R. S., Hopkins, P. F., Cox, T. J., Robertson, B. E., & Hernquist, L. 2008, MNRAS, 391, 481
Sturm, E., González-Alfonso, E., Veilleux, S., et al. 2011, ApJL, 733, 16
Szokoly, G. P., Bergeron, J., Hasinger, G., et al. 2004, ApJS, 155, 271
Tadhunter, C. 2008, MmSAI, 79, 1205
Taylor, E. N., Franx, M., van Dokkum, P. G., et al. 2009, ApJ, 694, 1171
Tremaine, S., Gebhardt, K., Bender, R., et al. 2002, ApJ, 574, 740
Tresse, L., Ilbert, O., Zucca, E., et al. 2007, A&A, 472, 403
Urrutia, T., Lacy, M., & Becker, R. H. 2008, ApJ, 674, 80
Whittle, M. 1992, ApJS, 79, 49
Willmer, C. N. A., Faber, S. M., Koo, D. C., et al. 2006, ApJ, 647, 853
Windhorst, R. A., Cohen, S. H., Hathi, N. P., et al. 2011, ApJS, 193, 27
Wuyts, S., Labbé, I., Schreiber, N. M. F., et al. 2008, ApJ, 682, 985
Xue, Y. Q., Brandt, W. N., Luo, B., et al. 2010, ApJ, 720, 368